Cell Reports

Article

Shootin1a-mediated actin-adhesion coupling generates force to trigger structural plasticity of dendritic spines

Graphical abstract

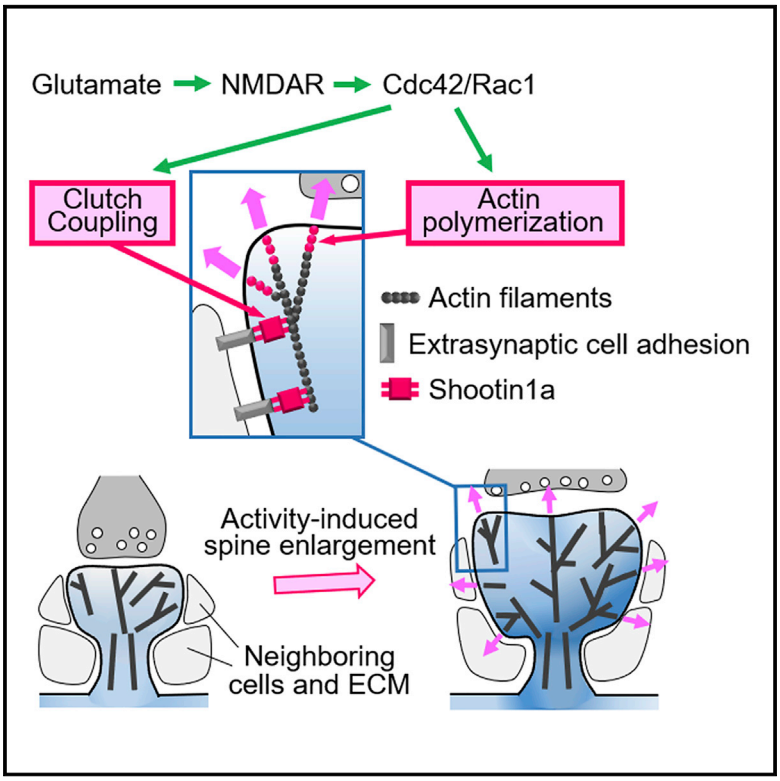

Highlights

- Shootin1a couples F-actin retrograde flow and cell adhesions in dendritic spines
- Synaptic activation enhances shootin1a-mediated clutch coupling in spines
- Shootin1a-mediated clutch coupling generates force for spine formation
- Activity-induced spine enlargement requires shootin1a-mediated clutch coupling

Authors

Ria Fajarwati Kastian, Takunori Minegishi, Kentarou Baba, ..., Singh Saranpal, Yasunori Hayashi, Naoyuki Inagaki

Correspondence

ninagaki@bs.naist.jp

In brief

Kastian et al. use gene knockout, protein interaction assays, force microscopy, and speckle imaging to analyze the molecular mechanics driving structural plasticity of dendritic spines. Their data demonstrate that both shootin1a-mediated clutch coupling and actin polymerization are required for the generation of force to trigger activity-induced spine enlargement.

Kastian et al., 2021, Cell Reports *35*, 109130
May 18, 2021
https://doi.org/10.1016/j.celrep.2021.109130

CellPress

Cell Reports

CellPress
OPEN ACCESS

Article

Shootin1a-mediated actin-adhesion coupling generates force to trigger structural plasticity of dendritic spines

Ria Fajarwati Kastian,[1,3] Takunori Minegishi,[1,3] Kentarou Baba,[1] Takeo Saneyoshi,[2] Hiroko Katsuno-Kambe,[1] Singh Saranpal,[1] Yasunori Hayashi,[2] and Naoyuki Inagaki[1,4,*]

[1]Laboratory of Systems Neurobiology and Medicine, Division of Biological Science, Nara Institute of Science and Technology, Ikoma, Nara 630-0192, Japan

[2]Department of Pharmacology, Kyoto University Graduate School of Medicine, Kyoto 606-8501, Japan

[3]These authors contributed equally

[4]Lead contact

*Correspondence: ninagaki@bs.naist.jp

https://doi.org/10.1016/j.celrep.2021.109130

SUMMARY

Dendritic spines constitute the major compartments of excitatory post-synapses. They undergo activity-dependent enlargement, which is thought to increase the synaptic efficacy underlying learning and memory. The activity-dependent spine enlargement requires activation of signaling pathways leading to promotion of actin polymerization within the spines. However, the molecular machinery that suffices for that structural plasticity remains unclear. Here, we demonstrate that shootin1a links polymerizing actin filaments in spines with the cell-adhesion molecules N-cadherin and L1-CAM, thereby mechanically coupling the filaments to the extracellular environment. Synaptic activation enhances shootin1a-mediated actin-adhesion coupling in spines. Promotion of actin polymerization is insufficient for the plasticity; the enhanced actin-adhesion coupling is required for polymerizing actin filaments to push against the membrane for spine enlargement. By integrating cell signaling, cell adhesion, and force generation into the current model of actin-based machinery, we propose molecular machinery that is sufficient to trigger the activity-dependent spine structural plasticity.

INTRODUCTION

Synapses have a pivotal role in the transmission and processing of information in the brain. Dendritic spines are tiny protrusions arising from dendrites that constitute the major compartments of excitatory post-synapses (Sheng and Hoogenraad, 2007; Bourne and Harris, 2008). These protrusive structures confer tunable properties on synaptic transmission. Dendritic spines undergo dynamic changes in size and shape during activity-dependent synaptic modification and behavioral learning (Yuste and Bonhoeffer, 2001; Lamprecht and LeDoux, 2004; Matsuzaki et al., 2004; Okamoto et al., 2004; Holtmaat and Svoboda, 2009; Roberts et al., 2010). Because the spine volume correlates positively with the amount of post- and presynaptic components as well as the amplitude of AMPA-receptor-mediated currents (Harris and Stevens, 1989; Matsuzaki et al., 2004; Hruska et al., 2018), the structural plasticity of spines is thought to be a key mechanism to change the synaptic efficacy underlying learning and memory (Yuste and Bonhoeffer, 2001; Holtmaat and Svoboda, 2009; Kasai et al., 2010; Bosch and Hayashi, 2012). The protrusive structure of spines also provides an isolated compartment for cell signaling that allows single synapses to be regulated as independent units (Müller and Connor, 1991; Inagaki et al., 2000; Yuste et al., 2000; Hayashi and Majewska, 2005; Lee et al., 2009; Murakoshi et al., 2011; Hedrick et al., 2016). In addition, dysregulation of the activity-dependent spine plasticity has been implicated in neuropsychiatric disorders, such as intellectual disability, autism spectrum disorder, and Alzheimer's disease (Kasai et al., 2010; Forrest et al., 2018).

Spines are enriched with dynamic actin cytoskeleton (Matus, 2000; Okamoto et al., 2004; Honkura et al., 2008; Korobova and Svitkina, 2010), and their structural plasticity requires cell signaling pathways that lead to actin polymerization within spines (Matus, 2000; Cingolani and Goda, 2008; Spence and Soderling, 2015; Lei et al., 2016). Intensive studies, including live imaging and loss-of-function analyses, have revealed that the actin-based spine plasticity is elicited by activation of NMDA-type glutamate receptors (NMDARs) and downstream signaling pathways, including Ca^{2+}, Ca^{2+}/calmodulin-dependent protein kinase II (CaMKII), Tiam1, Rac1, Cdc42, and p21-activated kinase (Pak) (Lamprecht and LeDoux, 2004; Hotulainen and Hoogenraad, 2010; Nishiyama and Yasuda, 2015; Saneyoshi et al., 2019). As the effectors of these pathways, regulators of the actin filament (F-actin) assembly/disassembly, such as the Arp2/3 complex, formins, profilin, and ADF/cofilin, have key roles in

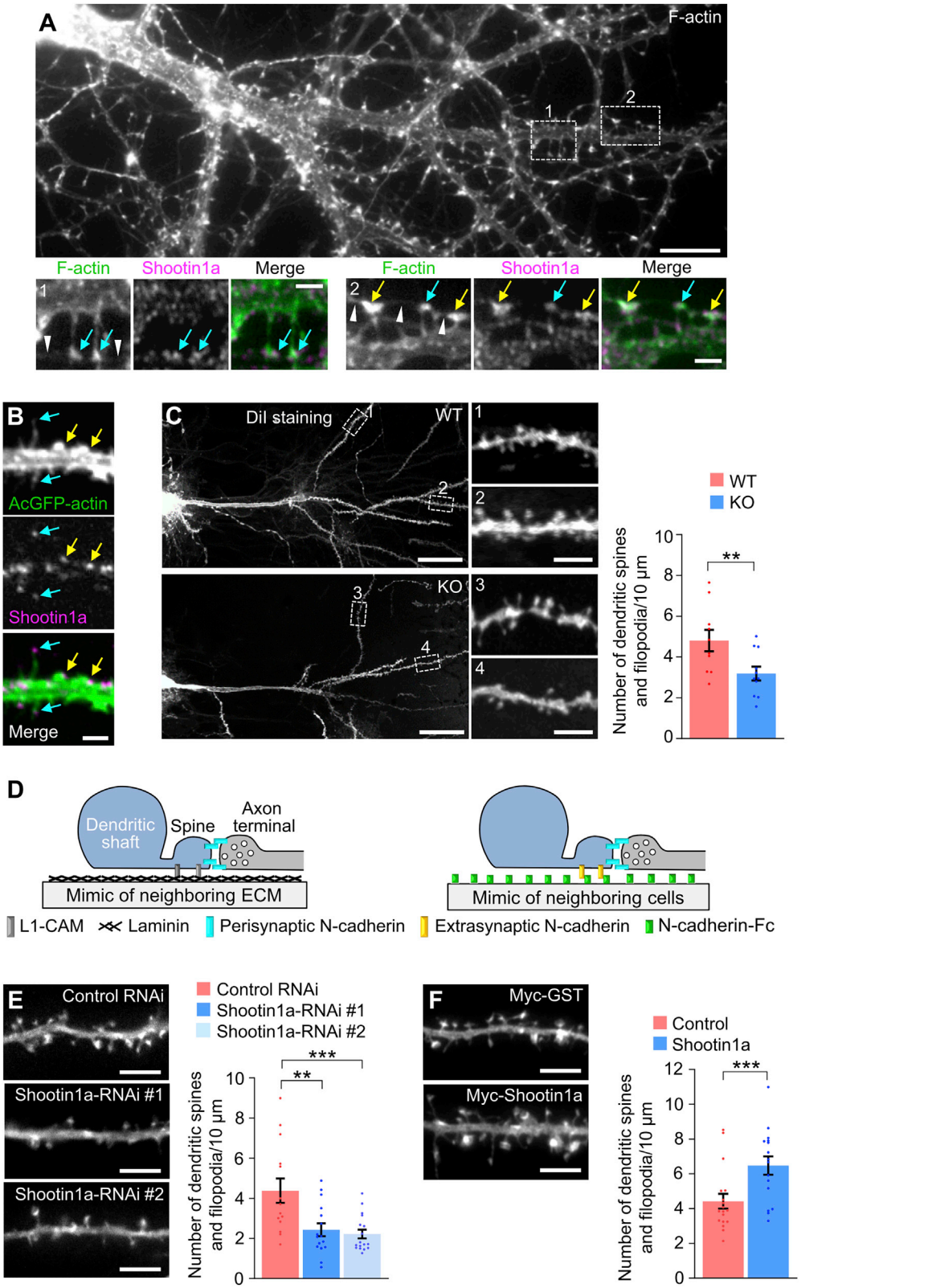

(legend on next page)

actin remodeling in the spines (Lamprecht and LeDoux, 2004; Nishiyama and Yasuda, 2015; Lei et al., 2016).

However, a fundamental question remains as to the spine plasticity. Spines in the brain are surrounded by a tightly packed environment, which includes axons, dendrites, glial processes, and the extracellular matrix (ECM) (Dityatev and Schachner, 2003; Sheng and Hoogenraad, 2007; Dansie and Ethell, 2011; Kasthuri et al., 2015). Thus, spine enlargement requires the generation of robust force to push not only against the spine membrane but also against the mechanical resistance of the extracellular environment. In addition, cell adhesion molecules and ECM proteins are involved in the formation and plasticity of spines (Arikkath and Reichardt, 2008; Bourne and Harris, 2008; Bozdagi et al., 2010; Dityatev et al., 2010; Dansie and Ethell, 2011; Hirano and Takeichi, 2012; Levy et al., 2014). However, current models of spine formation and plasticity do not incorporate mechanical force for spine enlargement, and thus, the molecular machinery that suffices for the activity-dependent spine structural plasticity remains unclear.

F-actins polymerize at the leading edge of axonal growth cones and motile cells, and disassemble proximally, thereby undergoing retrograde flow (Suter and Forscher, 2000; Pollard and Borisy, 2003). Recent studies using fluorescence photoactivation assays and single-molecule tracking analyses revealed a similar movement of actin molecules in dendritic spines (Honkura et al., 2008; Tatavarty et al., 2009; Frost et al., 2010). Although the directions of actin flow are more heterogeneous in spines than they are in growth cones, actin polymerization occurs mainly in the peripheral region and the net flow of F-actins is oriented from the periphery toward the center of the spines (Hotulainen et al., 2009; Frost et al., 2010; Tatavarty et al., 2012). Mechanical coupling between F-actin retrograde flow and cell adhesions by "clutch" molecules is thought to have a key role in generation of force for cell motility (Mitchison and Kirschner, 1988; Suter and Forscher, 2000; Toriyama et al., 2013). The actin-adhesion coupling (also referred to as "clutch coupling") produces traction forces on extracellular substrates and concurrently reduces the speed of the F-actin retrograde flow, thereby converting actin polymerization into the force that pushes the leading-edge membrane. However, the clutch molecule that reduces the F-actin retrograde flow for spine formation and enlargement remains unidentified.

Shootin1a is a clutch molecule involved in axon outgrowth and guidance (Toriyama et al., 2006; Baba et al., 2018). It produces traction force for growth-cone migration by mechanically coupling the F-actin retrograde flow to extracellular adhesive substrates (Kubo et al., 2015; Baba et al., 2018). Here, we demonstrate that shootin1a couples polymerizing F-actins in spines to the cell adhesion molecules N-cadherin and L1-CAM, thereby anchoring F-actins to the extracellular adhesive substrates as clutch molecules. Consistent with previous reports (Fukazawa et al., 2003; Matsuzaki et al., 2004; Okamoto et al., 2004), synaptic activation accelerated actin polymerization within the spines. In addition, we found that synaptic activation triggered Pak1-mediated shootin1a phosphorylation, which, in turn, enhanced the actin-adhesion coupling. When the shootin1a-mediated actin-adhesion coupling was disrupted, the accelerated actin polymerization was converted to an increase in actin retrograde flow, thereby hampering activity-dependent spine enlargement. By introducing shootin1a as a key clutch molecule, we propose molecular machinery that suffices for triggering activity-dependent spine structural plasticity.

RESULTS

Shootin1a is involved in dendritic spine formation

Consistent with the previously reported shootin1a expression in postnatal and adult mouse brains (Baba et al., 2018), immunoblot analysis detected shootin1a in 3–28 days *in vitro* (DIV) cultured rat hippocampal neurons (Figure S1A). Figure 1A shows shootin1a localization in a DIV14 cultured hippocampal neuron. Dendritic spines are categorized by morphology and maturation as thin, stubby, and mushroom spines and are thought to originate from dendritic filopodia (Bourne and Harris, 2008; Yuste, 2010). Shootin1a was detected in mushroom (Figure 1A, yellow arrows) and thin (blue arrows) spines and co-localized with the spine marker PSD-95 (Figure S1B). Shootin1a was also localized

Figure 1. Shootin1a is involved in dendritic spine formation

(A) A fluorescence image of a DIV 14 cultured rat-hippocampal neuron stained with Alexa-350 phalloidin for F-actin. Enlarged views of regions 1 and 2 in the rectangles co-stained with anti-shootin1a antibody are shown (bottom panel). Yellow and blue arrows indicate shootin1a localization in mushroom and thin spines, respectively. Arrowheads denote axons attached to those spines.

(B) A dendrite of a DIV 12 cultured rat-hippocampal neuron expressing aequorea coerulescens GFP (AcGFP)-actin and stained with anti-shootin1a antibody. Shootin1a is localized in stubby spines (yellow arrows) and dendritic filopodia (blue arrows).

(C) Hippocampal CA1 pyramidal neurons in P12 WT and shootin1 KO mouse brains labeled with DiI dye. Enlarged views of regions 1–4 in the rectangles are shown (right panel). The graph on the right shows a statistical analysis of the density of the dendritic spines and filopodia in apical dendrites. Two-tailed unpaired Student's t test; $p = 0.016$ (WT, n = 10 neurons, 1,494 spines; KO, n = 11 neurons, 1,110 spines).

(D) Schema of the adhesive substrates used in the present study. Neurons were cultured on glasses coated with PDL, PDL + laminin (left), or PDL + N-cadherin-Fc (right). Laminin and N-cadherin-Fc interact with L1-CAM and N-cadherin, respectively, in the extrasynaptic region of spines.

(E) Fluorescence images of the dendrites of DIV21 cultured rat-hippocampal neurons expressing control miRNA (control RNAi) or miRNA against shootin1a (shootin1a-RNAi 1 or 2); the neurons also co-express EGFP to visualize spines. The graph shows a statistical analysis of the density of the dendritic spines and filopodia. Two-tailed unpaired Welch's t test for $p = 0.0102$ (shootin1a-RNAi 1); Mann–Whitney U test for $p = 0.0014$ (shootin1a-RNAi 2) (control RNAi, n = 14 neurons, 3,439 spines; shootin1a-RNAi 1, n = 16 neurons, 2,868 spines; shootin1a-RNAi 2, n = 17 neurons, 2,039 spines).

(F) Fluorescence images of the dendrites of DIV21 cultured rat-hippocampal neurons overexpressing myc-GST (control) or myc-shootin1a (shootin1a). Neurons were also co-transfected with EGFP. The graph shows a statistical analysis of the density of dendritic spines and filopodia. Mann-Whitney U test; $p = 0.0063$ (control, n = 18 neurons, 2,821 spines; shootin1a, n = 16 neurons, 4,069 spines).

Data represent means ± SEM. *$p < 0.05$, **$p < 0.02$, ***$p < 0.01$. Scale bars: 20 μm for (A), top, and (C), left; 5 μm for (E) and (F); 3 μm for (C), right; 2 μm for (A), bottom, and (B). See also Figure S1.

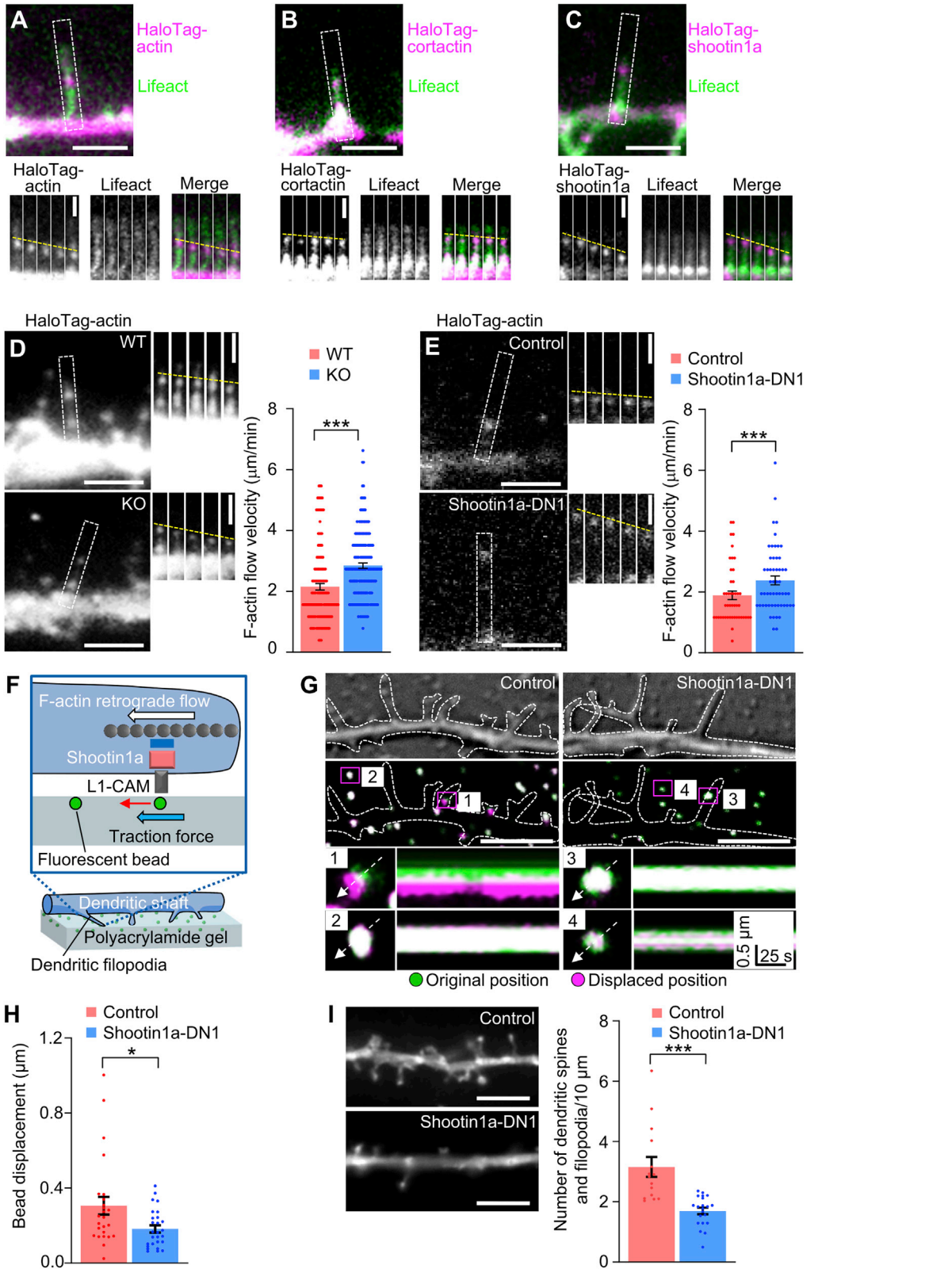

(legend on next page)

in stubby spines (Figure 1B, yellow arrows) as well as dendritic filopodia (blue arrows).

To elucidate the role of shootin1a in dendritic spines, pyramidal neurons in the hippocampus of postnatal day (P) 12 wild-type (WT) and shootin1 knockout (KO) mice (Baba et al., 2018) were labeled by 1,1′-dioctadecyl-3,3,3′,3′-tetramethyl-indocarbocyanine (DiI) dye (Figure 1C). In WT neurons, the density of dendritic spines and filopodia along the branches of apical dendrites was 4.81 ± 0.53 protrusions/10 μm (n = 10 cells), which is similar to previous data (Kirov et al., 2004) (Figure 1C). On the other hand, shootin1 KO neurons displayed a reduced density of spines and filopodia compared with the control (Figure 1C). In addition, shootin1 KO led to an increase in the percentage of dendritic filopodia and a decrease in the percentage of mushroom spines (Figure S1C). Because shootin1a is involved in axon outgrowth (Toriyama et al., 2013; Baba et al., 2018), the reduction in the density of dendritic spines and filopodia in shootin1 KO neurons might be an indirect effect of impaired axon outgrowth. To address that possibility, we sparsely transfected hippocampal neurons cultured on coverslips coated with the ECM protein laminin with miRNAs against shootin1a. Laminins have been detected around dendritic spines and implicated in the formation and stabilization of spines (Tian et al., 1997; Dityatev and Schachner, 2003; Omar et al., 2017). Thus, laminin-coated coverslips mimic an adhesive substrate presented on the ECM around spines (Figure 1D, left). Transfection efficiency was around 1.6%–2.0%, suggesting that the axon outgrowth of about 98% of the neurons is not affected in this assay. The density of dendritic spines and filopodia along the dendrites of GFP-positive transfected neurons was significantly decreased by RNAi on DIV 14 (Figure S1D) and DIV 21 (Figure 1E). On the other hand, overexpression of shootin1a, which was localized in dendritic spines and filopodia (Figure S1E), increased the density of spines and filopodia on DIV 4 (Figure S1F) and DIV 21 (Figure 1F). Together, these data demonstrate that shootin1a is involved in the formation of dendritic spines.

Shootin1a couples polymerizing F-actins in dendritic filopodia with the adhesive substrate

Next, we examined the mechanism underlying shootin1a-mediated spine formation. Consistent with previous data (Tatavarty et al., 2012), fluorescent speckle imaging analysis of HaloTag-actin detected F-actin retrograde flow in dendritic filopodia of the DIV 7 hippocampal neurons (Figure 2A, magenta; Video S1). F-actins in the dendritic filopodia were also monitored by Lifeact (Figure 2A, green). We previously reported that shootin1a interacts with the F-actin retrograde flow through its direct interaction with cortactin in the axonal growth cones (Kubo et al., 2015). Shootin1a also interacts with L1-CAM (Baba et al., 2018), which binds to laminin (Abe et al., 2018), thereby mechanically coupling the F-actin retrograde flow in growth cones with extracellular adhesive substrates. Immunocytochemical analyses showed colocalization of shootin1a with F-actin, cortactin, and L1-CAM in the dendritic filopodia (Figures S2A–S2C). Furthermore, HaloTag-cortactin and HaloTag-shootin1a expressed in the dendritic filopodia underwent retrograde movement (Figures 2B and 2C; Video S1), leading us to assume that shootin1a couples the F-actin retrograde flow in dendritic filopodia with adhesive substrates through its interaction with cortactin and L1-CAM (Figure S2D).

To investigate that possibility, we compared F-actin retrograde flow in dendritic filopodia of WT and shootin1 KO neurons cultured on laminin-coated dishes. F-actins polymerize mainly at the tip of dendritic filopodia (Hotulainen et al., 2009) and undergo retrograde flow (Figure S2D, white arrow); myosin II activity also contributes to

Figure 2. Shootin1a mediates actin-adhesion coupling for force generation and dendritic spine formation

(A–C) Fluorescent speckle images of HaloTag-actin (A), HaloTag-cortactin (B), and HaloTag-shootin1a (C) in dendritic filopodia of DIV7 rat-hippocampal neurons cultured on laminin-coated dishes. F-actins in dendritic filopodia were also monitored by Lifeact. See Video S1. Time-lapse montages of the indicated rectangular regions at 2-s intervals are shown to the right; dashed lines indicate the retrograde flow of speckles.

(D) Fluorescent speckle images of HaloTag-actin in dendritic filopodia of DIV7 hippocampal neurons prepared from WT and shootin1-KO mice and cultured on laminin-coated dishes. Time-lapse montages of the indicated rectangular regions at 2-s intervals are shown to the right; dashed lines indicate the retrograde flow of speckles. The graph shows a statistical analysis of F-actin flow velocity. Mann-Whitney U test; $p = 2.9 \times 10^{-10}$ (WT, n = 12 neurons, 38 spines, 142 speckles; KO, n = 11 neurons, 65 spines, 179 speckles).

(E) Fluorescent speckle images of HaloTag-actin in dendritic filopodia of DIV 7 cultured rat-hippocampal neurons overexpressing myc-GST (control) or myc-shootin1a-DN1 (shootin1a-DN1) and cultured on laminin-coated dishes. Time-lapse montages of the indicated rectangular regions at 2-s intervals are shown to the right; dashed lines indicate the retrograde flow of speckles. The graph shows a statistical analysis of F-actin flow velocity. Mann-Whitney U test; p = 0.0056 (control, n = 12 neurons, 17 spines, 46 speckles; shootin1a-DN1, n = 6 neurons, 17 spines, 55 speckles).

(F) Schema of traction force microscopy to monitor the force generated by the dendritic filopodia. Rat-hippocampal neurons were cultured on laminin-coated polyacrylamide gel embedded with fluorescent beads. Traction force under the filopodia (blue arrow) was monitored by visualizing force-induced deformation of the gel, which is reflected by the movement of beads under the filopodia (red arrow).

(G) Force measurement under the dendritic filopodia. Differential interference contrast (DIC) (top panels) and fluorescence (middle panels) images showing the dendritic filopodia of DIV 7 rat-hippocampal neurons overexpressing myc-GST (control) or myc-shootin1a-DN1 (shootin1a-DN1) and cultured on laminin-coated polyacrylamide gel embedded with 100-nm fluorescent beads. See Video S2. The pictures show representative images from the time-lapse series taken every 5 s for 125 s. The original and displaced positions of the beads in the gel are indicated by green and magenta colors, respectively. Dashed lines indicate the cell boundary. The four time-lapse montages (bottom panels) along the axis of the bead displacement (white dashed arrows) in the indicated areas show movement of the beads recorded every 5 s. The beads in areas 2 and 4 are reference beads.

(H) Statistical analysis of the magnitude of bead movement under dendritic filopodia overexpressing myc-GST or myc-shootin1a-DN1. Mann-Whitney U test; p = 0.022 (control, n = 25 beads, 22 filopodia, 5 neurons; shootin1a-DN1, n = 27 beads, 27 filopodia, 5 neurons).

(I) Fluorescence images of DIV 14 cultured rat-hippocampal neurons overexpressing myc-GST (control) or myc-shootin1a-DN1 (shootin1a-DN1). Neurons were also co-transfected with EGFP to visualize the spines. The graph shows a statistical analysis of the density of the dendritic spines and filopodia. Mann-Whitney U test; $p = 3.8 \times 10^{-6}$ (control, n = 15 neurons, 1,533 spines; shootin1a-DN1, n = 21 neurons, 951 spines).

Data represent means ± SEM. *p < 0.05, **p < 0.02, ***p < 0.01. Scale bars: 5 μm for (G) and (I); 2 μm for (A)–(C), top, and (D)–€, left; 1 μm for (A)–(C), bottom, and (D) and (E), right. See also Figure S2.

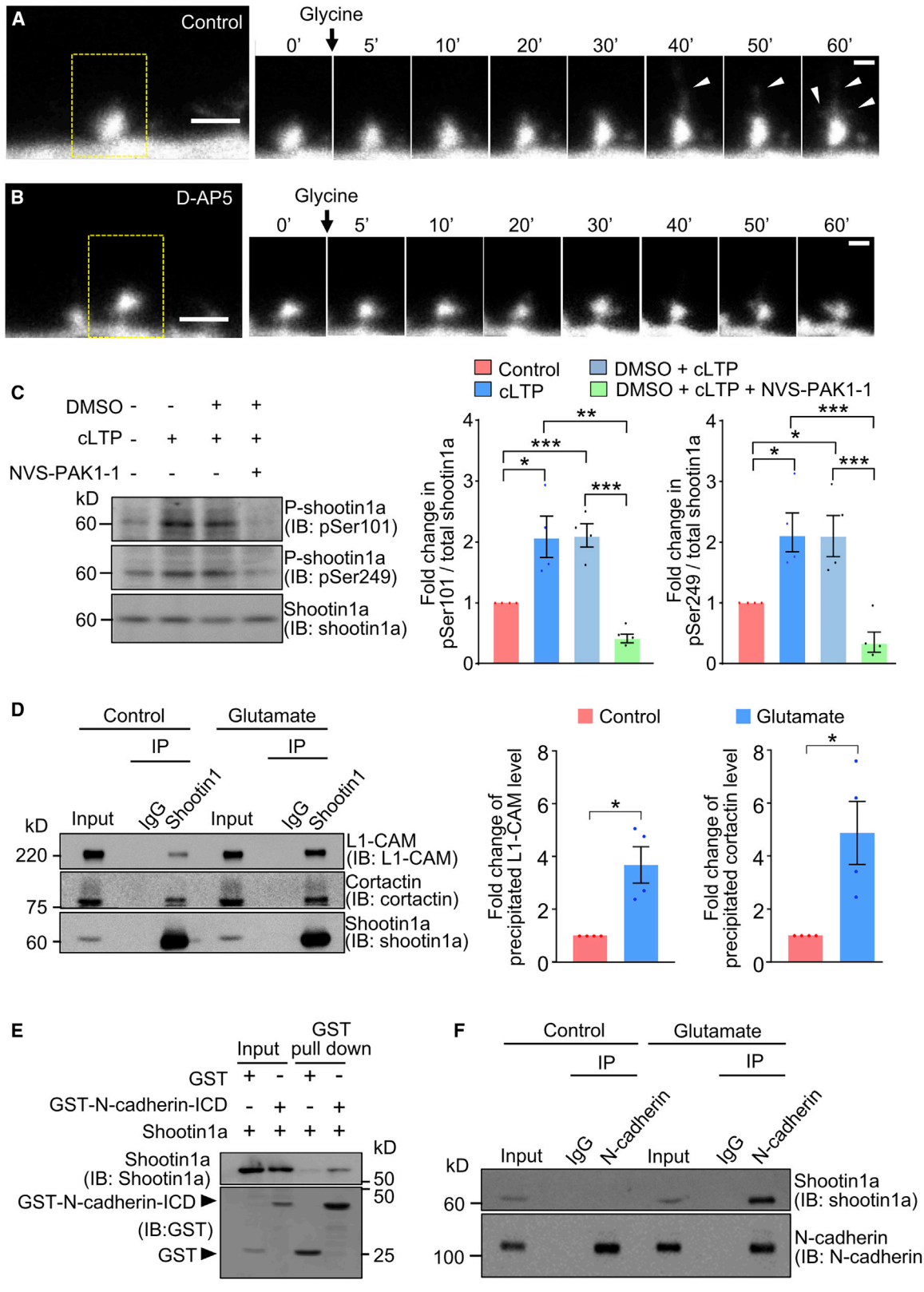

(legend on next page)

the flow (Tatavarty et al., 2012). If shootin1a contributes to the actin-adhesion coupling, the velocity of the F-actin flow should increase in the absence of shootin1a because of the decreased mechanical resistance to the F-actin flow (Suter and Forscher, 2000; Toriyama et al., 2013) (Figure S2E, white arrow). Indeed, the velocity of the actin flow increased in shootin1 KO neurons (Figure 2D). The actin flow velocity also increased by overexpression of a shootin1a dominant-negative mutant (shootin1a-DN1), shootin1a (1–125) (Baba et al., 2018), which disrupts the interaction between endogenous shootin1a and L1-CAM (Figure 2E). Hence, we conclude that shootin1a mediates the F-actin-adhesion coupling at the dendritic filopodia on laminin-coated substrates. It is notable that this F-actin-adhesion coupling is slippery because F-actin, cortactin, and shootin1a undergo retrograde movement even in the presence of shootin1a (Figures 2A–2C).

Shootin1a-mediated actin-adhesion coupling generates force for dendritic spine formation

If the F-actin flow is coupled with the adhesive substrates, the movement of the actin flow is transmitted to the substrate, thereby producing traction force on the substrate (Figure S2D, blue arrow). To analyze the role of shootin1a-mediated actin-adhesion coupling, we monitored the forces generated by dendritic filopodia, using traction-force microscopy. Hippocampal neurons were cultured on polyacrylamide gels coated with laminin; the gels were embedded with 100-nm fluorescent beads (Figures 2F and 2G, green circles). Forces under dendritic filopodia (Figure 2F, blue arrow) were monitored by visualizing force-induced deformation of the elastic substrate, which is reflected by movement of the beads from their original positions (red arrow) (Toriyama et al., 2013). Because of the tiny size of an individual filopodium, we could not find multiple beads under it. Therefore, the forces generated by filopodia are difficult to calculate by integrating the movements of multiple beads under them. Instead, we measured the magnitude and direction of the movement of individual beads under a filopodium (Figure 2G, magenta circles). The beads under the filopodia moved toward the dendritic shafts (Figures 2G and S2F; Video S2), indicating that the traction forces are exerted on the adhesive substrate. The magnitude of the bead movement was 0.31 ± 0.05 μm (n = 25) (Figure 2H). Consistent with our conclusion that shootin1a mediates actin-adhesion coupling (Figures S2D and S2E, blue arrows), the magnitude of the force represented by bead movement was significantly decreased when the interaction between shootin1a and L1-CAM was disrupted by shootin1a-DN1 (Figures 2G and 2H; Video S2). Furthermore, disruption of the actin-adhesion coupling by shootin1a-DN1 inhibited the formation of dendritic spines and filopodia (Figure 2I), indicating that shootin1a-mediated actin-adhesion coupling promotes the generation of force for dendritic spine formation.

Synaptic activation induces Pak1-mediated shootin1a phosphorylation, thereby enhancing shootin1a-L1-CAM, Shootin1a-cortactin, and Shootin1a-N-cadherin interactions

Stimulation of NMDARs activates Pak in dendritic spines (Hotulainen and Hoogenraad, 2010; Nishiyama and Yasuda, 2015). Because Pak1 phosphorylates shoootin1a at Ser101 and Ser249 (Toriyama et al., 2013), we next examined whether synaptic activation affects shootin1a phosphorylation by immunoblot analysis. Stimulation of cultured hippocampal neurons by 10 μM glutamate significantly increased shootin1a phosphorylation at Ser249, and the phosphorylation was inhibited in the presence of a Pak1 inhibitor, NVS-PAK1-1 (Figure S3A). To further analyze shootin1a phosphorylation during synaptic activation, we performed chemical long-term potentiation (cLTP) on laminin-coated dishes. Synaptic NMDARs of hippocampal neurons expressing EGFP were activated by glycine treatment (Lu et al., 2001; Park et al., 2004). Consistent with a previous report (Hruska et al., 2018), 54% of spines (n = 158) enlarged during the cLTP procedure (Figures 3A and S3B; Video S3). During synaptic activation, spines underwent dynamic changes in morphology;

Figure 3. Synaptic activation induces pak1-mediated shootin1a phosphorylation, thereby enhancing shootin1a-l1-cam, shootin1a-cortactin, and shootin1a-N-cadherin interactions

(A and B) Fluorescence time-lapse images of dendritic spines of DIV 14 rat-hippocampal neurons expressing EGFP in the absence (A) and presence (B) of 50 μM D-AP5 (NMDAR antagonist); time-lapse images of the indicated rectangular regions are shown to the right. Neurons were cultured on laminin-coated dishes. cLTP was induced by 200 μM glycine (arrows) in the absence of Mg^{2+}. Arrowheads in (A) indicate protrusive structures induced by cLTP. See Video S3. The time courses of spine-volume changes during cLTP are shown in Figures S3B and S3D.

(C) DIV 14 hippocampal neurons were stimulated with or without (control) 200 μM glycine for 30 min in the absence of Mg^{2+}. To inhibit Pak1, 0.25 μM NVS-PAK1-1 was applied 30 min before the glycine stimulation. Cell lysates were analyzed by immunoblot with anti-pSer101-shootin1a, anti-pSer249-shootin1a, and anti-shootin1a antibodies. The left graph shows quantitative data for phosphorylated shootin1a at Ser101. Two-tailed unpaired Welch's t test. p = 0.0477 (control versus cLTP), p = 0.0099 (control versus DMSO + cLTP), p = 0.0139 (cLTP versus DMSO + cLTP + NVS-PAK1-1), p = 0.0014 (DMSO + cLTP versus DMSO + cLTP + NVS-PAK1-1) (n = 4 independent experiments). The right graph shows quantitative data for phosphorylated shootin1a at Ser249. Two-tailed unpaired Welch's t test. p = 0.0382 (control versus cLTP), p = 0.0464 (control versus DMSO + cLTP), p = 0.0063 (cLTP versus DMSO + cLTP + NVS-PAK1-1), p = 0.0078 (DMSO + cLTP versus DMSO + cLTP + NVS-PAK1-1) (n = 4 independent experiments).

(D) Co-immunoprecipitation of L1-CAM and cortactin with shootin1a in DIV 14 cultured rat cortical neurons. After incubation of neurons with 10 μM glutamate or medium (control) for 30 min, cell lysates were prepared and incubated with anti-shootin1 antibody for immunoprecipitation. The immunoprecipitates were immunoblotted with anti-shootin1a, anti-L1-CAM, and anti-cortactin antibodies. Right graphs show quantitative data for bound L1-CAM and bound cortactin. Two-tailed unpaired Welch's t test. p = 0.030 (precipitated L1-CAM), p = 0.047 (precipitated cortactin) (n = 4 independent experiments).

(E) *In vitro* binding assay using purified shootin1a and purified GST-N-cadherin ICD. Shootin1a (300 nM) was incubated with GST-N-cadherin (300 nM) and glutathione sepharose 4B. GST-N-cadherin was then eluted. After SDS-PAGE, the eluates were immunoblotted with anti-shootin1a or anti-GST antibody.

(F) Co-immunoprecipitation of shootin1a with N-cadherin in DIV 14 cultured rat cortical neurons. After incubation of neurons with 10 μM glutamate or medium (control) for 30 min, cell lysates were prepared and incubated with anti-N-cadherin antibody for immunoprecipitation. The immunoprecipitates were immunoblotted with anti-N-cadherin and anti-shootin1a antibodies. Representative data of similar individual results (n = 3) are shown.

Data represent means ± SEM. *p < 0.05, **p < 0.02, ***p < 0.01, ns, not significant. Scale bars: 2 μm for (A) and (B), left; 1 μm for (A) and (B), right. See also Figures S3–S5.

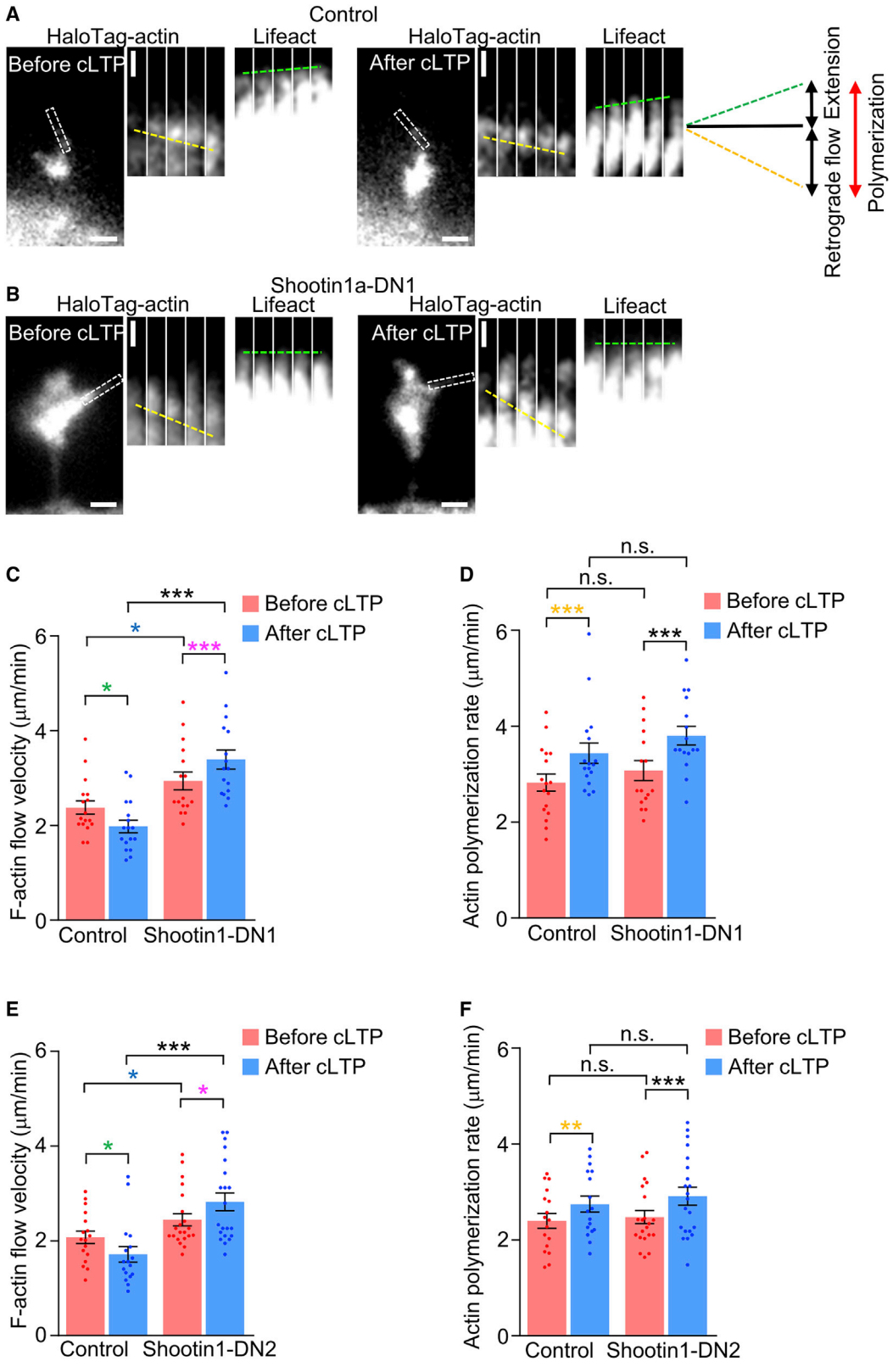

(legend on next page)

we often observed finger-like protrusions, and ruffles emanated from spine heads, as reported (Honkura et al., 2008; Chazeau et al., 2014) (Figure 3A, arrowheads). Both the NMDAR antagonists D-AP5 (D-2-amino-5-phosphonovalerate) (50 μM) and MK-801 (10 μM) inhibited the glycine-induced spine enlargement (Figures 3B, S3C, and S3D; Video S3), confirming that the structural plasticity is NMDAR dependent (Hruska et al., 2018). The activation of NMDARs by glycine treatment also increased shootin1a phosphorylation at Ser101 and Ser249, and the phosphorylation was inhibited by NVS-PAK1-1 (Figure 3C), thereby indicating that synaptic activation induces Pak1-mediated shootin1a phosphorylation.

We previously reported that Pak1-mediated shootin1a phosphorylation enhances shootin1a-L1-CAM and shootin1a-cortactin interactions (Kubo et al., 2015; Baba et al., 2018). To examine whether synaptic activation affects shootin1a-L1-CAM and shootin1a-cortactin interactions in cultured hippocampal neurons, neurons were stimulated by glutamate to increase the level of shootin1a phosphorylation. Shootin1a in the cell lysates was then immunoprecipitated by an anti-shootin1 antibody. The amounts of L1-CAM and cortactin that co-precipitated with shootin1a were significantly increased by the glutamate application (Figure 3D), demonstrating that glutamate stimulation enhances shootin1a-cortactin and shootin1a-L1-CAM interactions.

N-cadherin has key roles in dendritic spine plasticity (Togashi et al., 2002; Bozdagi et al., 2010; Hirano and Takeichi, 2012), and previous studies, including immunoelectron microscopic analyses, reported N-cadherin localization not only in the perisynaptic region but also in the extrasynaptic region of the dendritic spines (Uchida et al., 1996; Okamura et al., 2004; Korobova and Svitkina, 2010). Consistent with those observations, we detected signals of N-cadherin in the extrasynaptic region (Figure S4A, yellow arrowheads) as well as in the perisynaptic region (blue arrowheads) of spine heads. Interestingly, *in vitro* binding analysis demonstrated that shootin1a directly interacts with the intracellular domain (ICD) of N-cadherin (Figure 3E); binding assays with shootin1a-deletion mutants also showed that residues 30–146 of shootin1a (shootin1a [30–146]) are sufficient to bind to N-cadherin-ICD (Figure S4B). Hence, in addition to L1-CAM, extrasynaptic N-cadherin might link shootin1a and adhesive substrates for actin-adhesion coupling in dendritic spines (Figure S5A). We further examined whether glutamate stimulation affects shootin1a-N-cadherin interaction in cultured hippocampal neurons. In control neurons, we could not detect shootin1a co-precipitated with N-cadherin (Figure 3F). On the other hand, a considerable amount of shootin1a co-precipitated with N-cadherin after neuronal stimulation by glutamate (Figure 3F), indicating that glutamate stimulation enhances shootin1a-N-cadherin interaction.

Synaptic activation enhances shootin1a-mediated actin-adhesion coupling in dendritic spines

The enhancements of shootin1a-cortactin, shootin1a-L1-CAM, and shootin1a-N-cadherin interactions by glutamate raise the possibility that synaptic activation promotes shootin1a-mediated actin-adhesion coupling in dendritic spines (Figure S5B). To examine that possibility, we monitored actin dynamics within dendritic spines of neurons cultured on laminin-coated dishes (Figure 1D, left). Consistent with previous reports (Hotulainen et al., 2009; Chazeau et al., 2014), fluorescent speckles of HaloTag-actin moved from the periphery to the center of the spine heads (Figure S6A;Video S4). HaloTag-cortactin and HaloTag-shootin1a also underwent centripetal movement (Figures S6B and S6C). F-actin flow velocity was calculated by tracing the speckles of the HaloTag actin (Figure 4A, yellow lines). The actin polymerization rate was calculated as the sum (Figure 4A, red arrow) of the F-actin protrusion rate, monitored by Lifeact (green lines) and the F-actin flow velocity (yellow lines). Importantly, disruption of the shootin1a-L1-CAM interaction by shootin1a-DN1 increased the velocity of the F-actin flow in the spines (Figures 4A and 4B; see blue asterisks in Figure 4C), indicating that shootin1a-L1-CAM interaction also mediates the F-actin-adhesion coupling in the dendritic spines (Figure S5A).

In control spines, cLTP induction increased the actin polymerization rate (0.62 ± 0.39 μm/min increase; Figure 4A; see yellow asterisk in Figure 4D), consistent with previous reports that

Figure 4. Synaptic activation promotes actin polymerization and shootin1a-mediated actin-adhesion coupling in dendritic spines

(A and B) Fluorescent speckle images of HaloTag-actin and fluorescence images of Lifeact in dendritic spines of DIV 14 rat-hippocampal neurons overexpressing myc-GST (control) (A) or myc-shootin1a-DN1 (shootin1a-DN1) (B) and cultured on laminin-coated dishes. Images were taken before (left) and after (right) cLTP induction by glycine (200 μM, 4 min). Time-lapse montages of the indicated rectangular regions at 2-s intervals are shown to the right. Yellow and green dashed lines indicate HaloTag-actin retrograde flow and F-actin extension, respectively. The actin polymerization rate (red arrow) was calculated as the sum of the actin retrograde flow and the F-actin extension rates.

(C and D) F-actin flow velocity (C) and actin polymerization rate (D) calculated from the time-lapse montage analyses in (A) and (B). Two-tailed paired t test for (C), $p = 0.025$ (before cLTP versus after cLTP in control), $p = 0.0047$ (before cLTP versus after cLTP in shootin1a-DN1). For (D), $p = 3.9 \times 10^{-4}$ (before cLTP versus after cLTP in shootin1a-DN1). Wilcoxon signed-rank test for (D), $p = 0.0075$ (before cLTP versus after cLTP in control). Two-tailed unpaired Student's t test for (C), $p = 0.023$ (before cLTP in control versus before cLTP in shootin1a-DN1), $p = 1.7 \times 10^{-6}$ (after cLTP in control versus after cLTP in shootin1a-DN1). For (D), $p = 0.364$ (before cLTP in control versus before cLTP in shootin1a-DN1). Mann-Whitney U test for (D), $p = 0.064$ (after cLTP in control versus after cLTP in shootin1a-DN1) (control, n = 17 neurons, 17 spines; shootin1a-DN1, n = 16 neurons, 16 spines).

(E and F) F-actin flow velocity (E) and F-actin polymerization rate (F) calculated from fluorescent speckle images of HaloTag-actin and fluorescence images of Lifeact in dendritic spines of DIV 14 rat-hippocampal neurons overexpressing myc-GST (control) or myc-shootin1a-DN2 (shootin1a-DN2) and cultured on dishes coated with N-cadherin-Fc. Wilcoxon signed-rank test for (E), $p = 0.013$ (before cLTP versus after cLTP in control). Two-tailed paired t test for (E), $p = 0.030$ (before cLTP versus after cLTP in shootin1a-DN2). For (F), $p = 0.013$ (before cLTP versus after cLTP in control), $p = 0.0035$ (before cLTP versus after cLTP in shootin1a-DN2). Two-tailed unpaired Student's t test for (E), $p = 0.029$ (before cLTP in control versus before cLTP in shootin1a-DN2). For (F), $p = 0.624$ (before cLTP in control versus before cLTP in shootin1a-DN2), $p = 0.695$ (after cLTP in control versus after cLTP in shootin1a-DN2). Mann-Whitney U test for (E), $p = 2.1 \times 10^{-5}$ (after cLTP in control versus after cLTP in shootin1a-DN2). (Control, n = 18 neurons, 18 spines; shootin1a-DN2, n = 22 neurons, 22 spines).

Data represent means ± SEM. *$p < 0.05$, **$p < 0.02$, ***$p < 0.01$, ns, not significant. Scale bars: 1 μm for (A) and (B), left; 0.5 μm for (A) and (B), right. See also Figures S5–S7.

activity-dependent spine enlargement is accompanied by actin polymerization (Okamoto et al., 2004). At the same time, the velocity of the F-actin retrograde flow was significantly reduced by cLTP (0.40 ± 0.27 μm/min decrease; Figure 4A; see green asterisks in Figure 4C). This is consistent with a previous observation that synaptic activation by glutamate uncaging decreased the pool of F-actins that undergo retrograde flow (Honkura et al., 2008) and indicates that actin-adhesion coupling is enhanced by synaptic activation (Figure S5B). To determine whether shootin1a mediates the increased actin-adhesion coupling, we monitored F-actin flow in the spines of neurons overexpressing shootin1a-DN1. If shootin1a mediates the increased actin-adhesion coupling, blockade of shootin1a function should lead to an increase in F-actin retrograde flow rate during cLTP. Namely, in the absence of the increased actin-adhesion coupling, an increase in the actin polymerization rate should be converted to an increase in the F-actin retrograde flow rate (Figure S5C, white arrow). Indeed, in the presence of shootin1a-DN1, the F-actin retrograde flow rate in spines increased upon cLTP induction (Figure 4B; see magenta asterisks in Figure 4C). The increases in the actin polymerization rate and F-actin retrograde flow velocity were 0.72 ± 0.40 μm/min and 0.45 ± 0.39 μm/min, respectively, indicating that 63% of the increased actin polymerization was converted to F-actin retrograde flow when shootin1a-L1-CAM interaction was disrupted.

To determine whether N-cadherin also mediates the coupling between shootin1a and adhesive substrates, we monitored actin dynamics within dendritic spines of neurons cultured on dishes coated with N-cadherin-Fc. N-cadherin-Fc-coated dishes mimic an adhesive substrate presented on the extrasynaptic neighboring cells (Figure 1D, right). For that purpose, we designed another shootin1a dominant-negative mutant, shootin1a-DN2, which disrupts the shootin1a-N-cadherin interaction (Figure S7). We obtained essentially the same results for F-actin retrograde flow and actin polymerization as above, during cLTP induction, in control neurons and in neurons overexpressing shootin1a-DN2 (Figures 4E and 4F). The increase in the actin polymerization rate and the decrease in the F-actin retrograde flow velocity in control neurons during cLTP were 0.42 ± 0.32 μm/min and 0.37 ± 0.28 μm/min, respectively. The increases in the actin polymerization rate and the F-actin retrograde flow velocity in neurons expressing shootin1a-DN2 during cLTP were 0.42 ± 0.31 μm/min and 0.34 ± 0.31 μm/min, respectively, indicating that 81% of the increased actin polymerization was converted to F-actin retrograde flow when shootin1a-N-cadherin interaction was disrupted. These data indicate that extrasynaptic N-cadherin mediates the coupling between shootin1a and adhesive substrates, thereby contributing to the enhancement of shootin1a-mediated actin-adhesion coupling (Figure S5B). Together, these results demonstrate that synaptic activation promotes not only actin polymerization but also shootin1a-mediated actin-adhesion coupling via activity-dependent shootin1a interactions with L1-CAM and N-cadherin.

Spine structural plasticity requires shootin1a and shootin1a phosphorylation

Synaptic activation induced Pak1-mediated shootin1a phosphorylation; this, in turn, enhanced shootin1a-mediated actin-adhesion coupling. To examine the role of that enhancement, we next analyzed the effect of shootin1a phosphorylation. To do so, we transfected hippocampal neurons cultured on laminin-coated dishes (Figure 1D, left) with miRNA against shootin1a. As shown in Figures 5A, 5B, and 5F, repression of shootin1a by shootin1a miRNA completely inhibited the spine enlargement induced by the glycine treatment. In addition, expression of WT RNAi-refractory shootin1a (shootin1a-WT) in neurons expressing shootin1a miRNA rescued the inhibition of spine enlargement (Figures 5B, 5C, and 5F), indicating that shootin1a is required for spine enlargement during the cLTP procedure. Furthermore, the inhibition of spine enlargement was rescued by phosphomimic shootin1a (shootin1a-DD), in which both Ser101 and Ser249 were replaced with aspartate (Toriyama et al., 2013) (Figures 5B, 5D, and 5G). However, unphosphorylated shootin1 (shootin1-AA), in which those residues were replaced with alanine (Toriyama et al., 2013), could not rescue the spine enlargement (Figures 5B, 5E, and 5G), indicating that shootin1a phosphorylation elicited by synaptic activation is required for the spine enlargement during the cLTP procedure.

Spine structural plasticity requires shootin1a-mediated actin-adhesion coupling

Finally, we examined the role of shootin1a-mediated actin-adhesion coupling in spine structural plasiticity. Notably, we observed spine enlargement during the cLTP procedure on dishes coated with laminin or N-cadherin-Fc (Figures 1D and 6A) but not on the dishes coated only with poly-D-lysine (PDL) (Figure 6A), indicating that the structural plasticity of dendritic spines associated with cLTP requires the adhesive substrates that are involved in shootin1a-mediated actin-adhesion coupling (Figure S5A). Furthermore, disruption of the shootin1a-L1-CAM interaction by shootin1a-DN1 abolished spine enlargement during the cLTP procedure on laminin (Figure 6B). Similarly, disruption of the shootin1a-N-cadherin interaction by shootin1a-DN2 inhibited spine enlargement on N-cadherin-Fc (Figure 6C). These data indicate that shootin1a-mediated actin-adhesion coupling is required for the spine plasticity during cLTP.

In the brain, dendritic spines are surrounded by various tissue components, including axons, dendrites, glial processes, and the ECM, which provide adhesive substrates (Dityatev and Schachner, 2003; Sheng and Hoogenraad, 2007; Kasthuri et al., 2015). To examine the role of shootin1a in structural plasticity of dendritic spines *in situ*, we performed two-photon glutamate-uncaging stimulation in rat hippocampal organotypic slice cultures. Single spines of CA1 pyramidal neurons, co-expressing EGFP with control microRNA (miRNA) or shootin1a miRNA, were stimulated by glutamate uncaging (Figure 7A, asterisks). Consistent with previous reports (Matsuzaki et al., 2004; Bosch et al., 2014), 30-s stimulation of control spines by glutamate uncaging induced their rapid enlargement, which was followed by dynamic fluctuation in size (Figure 7A; Video S5). On average, the spine enlargement persisted for more than 30 min (Figure 7B). That rapid and sustained enlargement of spines is called structural LTP (Bosch et al., 2014; Hedrick et al., 2016). During structural LTP, spines underwent dynamic movement, and we often observed ruffling that emanated from

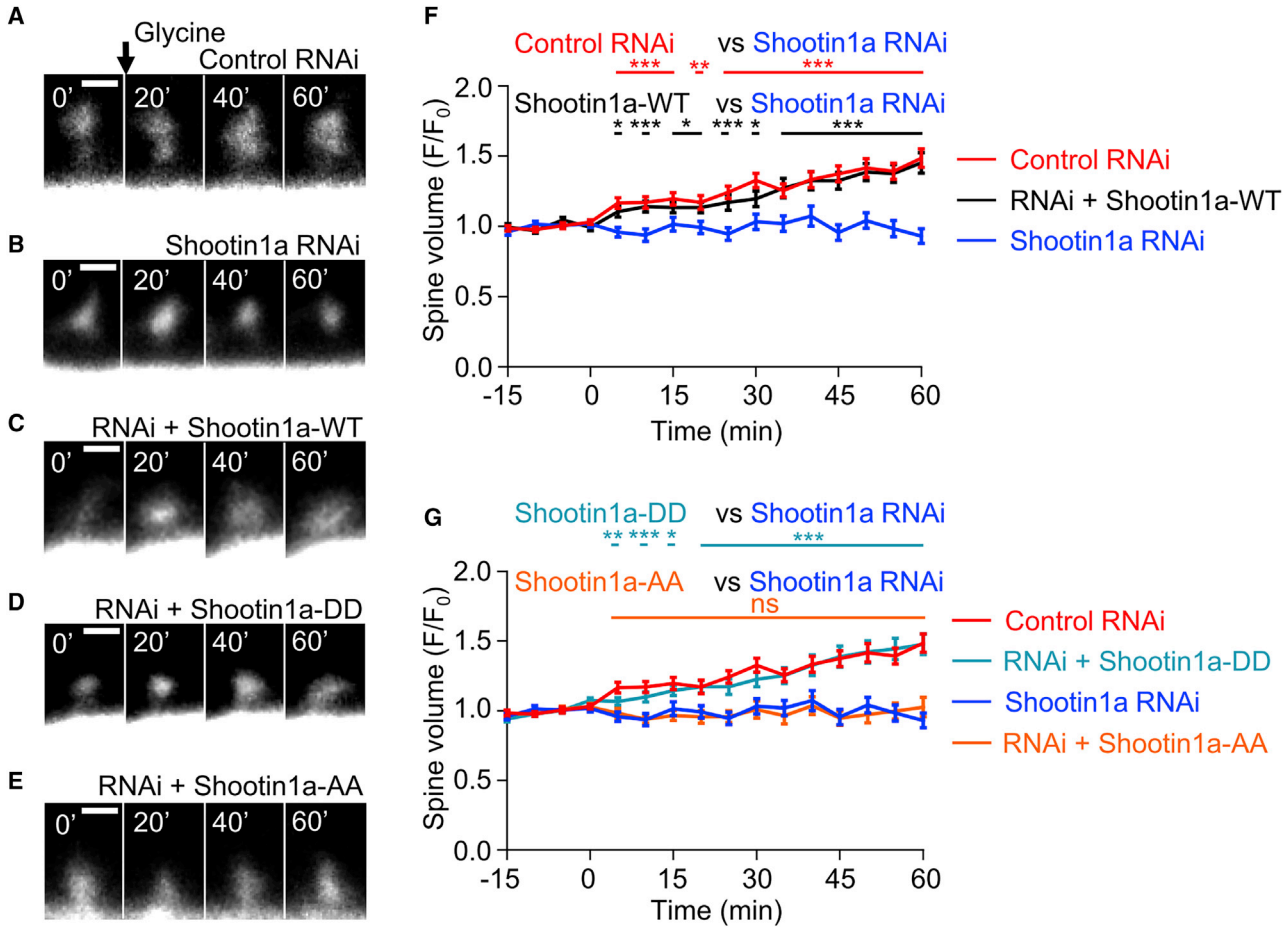

Figure 5. Spine structural plasticity requires shootin1a and shootin1a phosphorylation

(A–E) Fluorescence time-lapse images of dendritic spines of DIV 14 rat-hippocampal neurons expressing EGFP during cLTP induction. Neurons expressing control miRNA (A), shootin1 miRNA 1 (B), shootin1 miRNA 1 + RNAi-refractory shootin1a-WT (C), shootin1 miRNA 1 + RNAi-refractory shootin1a-DD (D), or shootin1 miRNA 1 + RNAi-refractory shootin1a-AA (E) were stimulated with 200 μM glycine in the absence of Mg^{2+}.

(F and G) Time courses of spine volume changes during cLTP in (A)–(C) and (A), (B), (D), and (E). The spine volumes were calculated by measuring the total fluorescence intensity (F) of spine heads relative to the averaged baseline fluorescence intensity (F_0), and were compared with the average of spine volumes before cLTP induction (−15 to 0 min). Control RNAi, n = 8 neurons, 62 spines; shootin1a RNAi, n = 9 neurons, 58 spines; RNAi + shootin1a-WT, n = 9 neurons, 74 spines; RNAi + shootin1a-DD, n = 9 neurons, 65 spines; RNAi + shootin1a-AA, n = 8 neurons, 63 spines. The results of the significance test are summarized in Data S1.

Data represent means ± SEM. *p < 0.05, **p < 0.02, ***p < 0.01, ns, not significant. Scale bars: 1 μm.

spine heads, as reported (Honkura et al., 2008) (Figure 7A, arrowheads). Downregulation of shootin1a by RNAi significantly inhibited the spine enlargement at early (1–2 min) and late (21–31 min) phases (Figures 7A–7C; Video S6). Furthermore, expression of RNAi-refractory shootin1a rescued the reduction of the spine enlargement (Figures 7A–7C; Video S7), thereby indicating that shootin1a has an essential role in spine structural LTP in brain tissue. Together, these data demonstrate that shootin1a-mediated actin-adhesion coupling is required for spine structural plasticity.

DISCUSSION

The present study demonstrated that shootin1a links polymerizing actin filaments in spines with N-cadherin and L1-CAM, thereby mechanically coupling actin filaments to extracellular adhesive substrates (Figure 7D). Traction force microscopy revealed that shootin1a-mediated actin-adhesion coupling generates force for spine formation. Consistent with previous findings (Fukazawa et al., 2003; Matsuzaki et al., 2004; Okamoto et al., 2004), synaptic activation promoted actin polymerization within spines (Figure 7D, blue arrow). Concurrently, synaptic activation induced Pak1-mediated shootin1a phosphorylation, which in turn enhanced actin-adhesion coupling (Figure 7D, red arrow). The enhanced actin-adhesion coupling reduced the speed of the F-actin retrograde flow (white arrows), thereby increasing the efficiency of the conversion of the actin polymerization into a force that pushes the spine membrane (pink arrows). When the actin-adhesion coupling was disrupted (Figure 7E), a large proportion of actin polymerization promoted by the synaptic

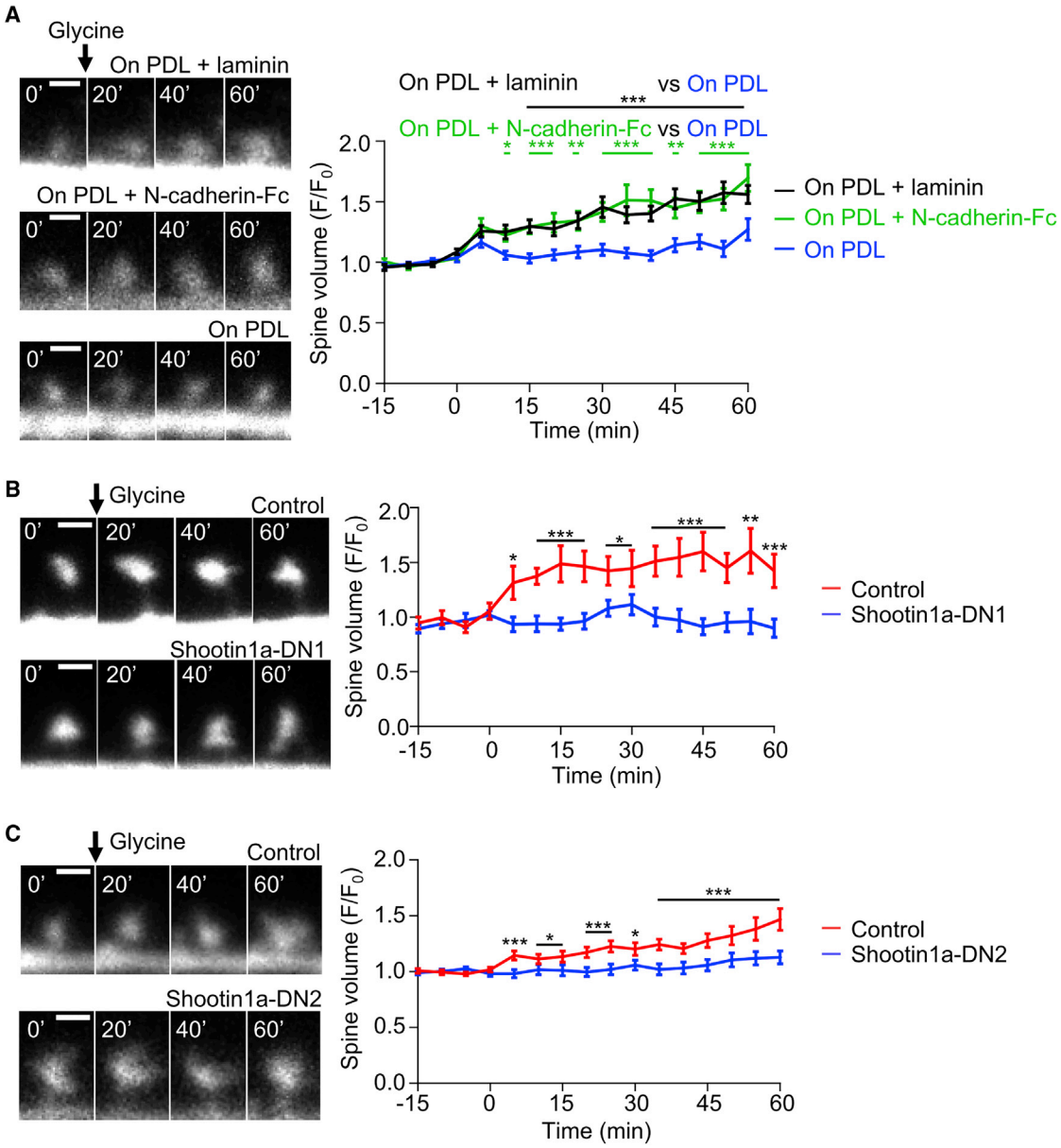

Figure 6. Spine structural plasticity requires shootin1a-mediated actin-adhesion coupling

(A) Fluorescence time-lapse images of dendritic spines (left) and time course of their volume changes (right) of DIV 14 rat-hippocampal neurons expressing EGFP. cLTP was induced by 200 μM glycine in the absence of Mg^{2+}. On PDL, n = 6 neurons, 54 spines; on PDL + laminin, n = 7 neurons, 86 spines; on PDL + N-cadherin-Fc, n = 5 neurons, 56 spines.

(B) Fluorescence time-lapse images of dendritic spines (left) and time course of their volume changes (right) of DIV 14 rat-hippocampal neurons expressing EGFP. Neurons were cultured on laminin-coated dishes and overexpressed myc-GST (control) or myc-shootin1a-DN1 (shootin1a-DN1). Control, n = 3 neurons, 15 spines; shootin1a-DN1, n = 4 neurons, 14 spines.

(C) Fluorescence time-lapse images of dendritic spines (left) and time course of their volume changes (right) of DIV 14 rat-hippocampal neurons expressing EGFP. Neurons were cultured on N-cadherin-Fc-coated dishes and overexpressed myc-GST (control) or myc-shootin1a-DN2 (shootin1a-DN2). Control, n = 8 neurons, 74 spines; shootin1a-DN2, n = 8 neurons, 80 spines.

The results of the significance test are summarized in Data S1. Data represent means ± SEM. *p < 0.05, **p < 0.02, ***p < 0.01, ns, not significant. Scale bars: 1 μm.

activation (Figure 7E, asterisks) was converted to an increase in actin retrograde flow (white arrow), thereby hampering the activity-dependent spine enlargement. The shootin1a-RNAi-mediated disruption of actin-adhesion coupling was rescued by shootin1a-DD, but not by shootin1a-AA (Figure 5G), indicating that the activated form of shootin1a is required for the cLTP. In this condition, actin-adhesion coupling does not change (i.e., is always active) but actin polymerization is promoted under the

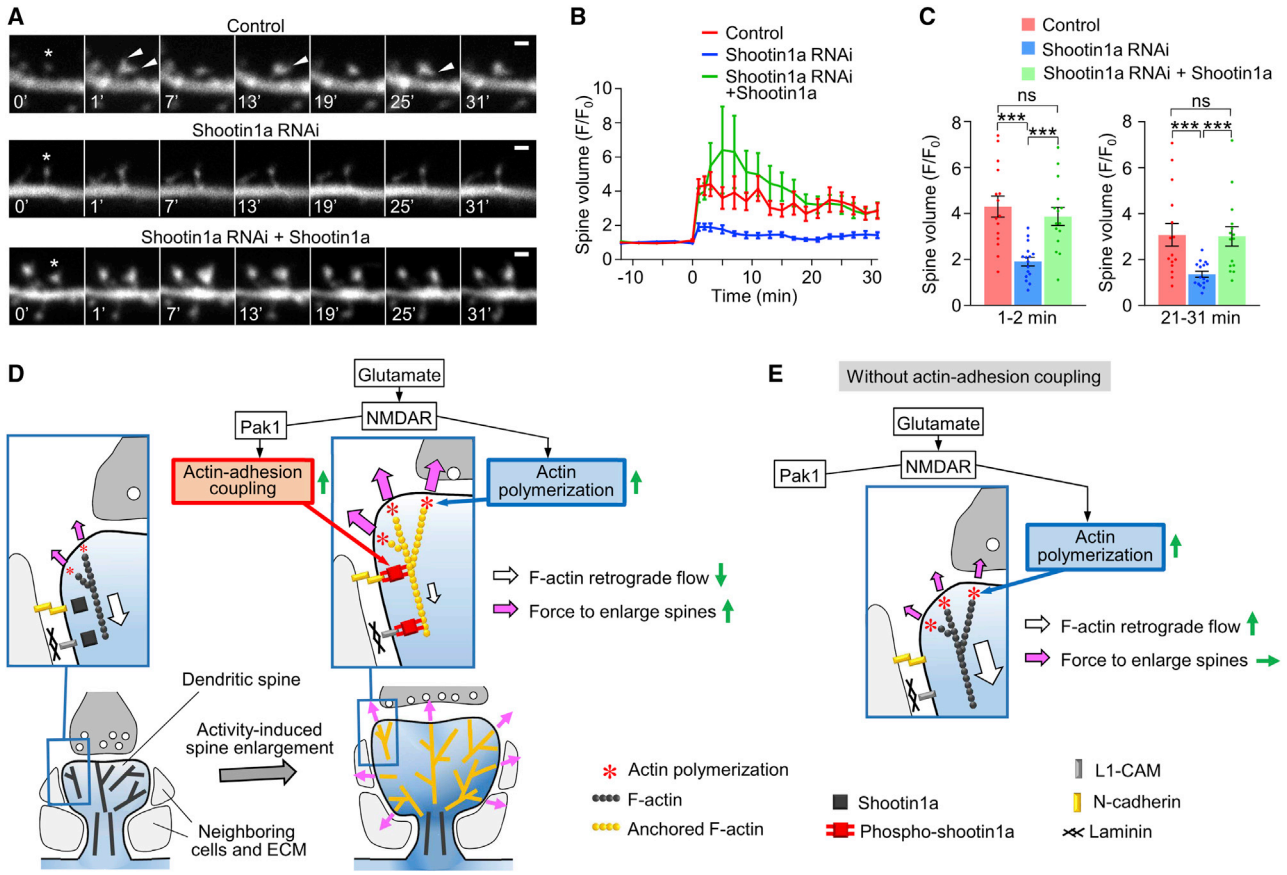

Figure 7. Shootin1a is required for spine structural plasticity in hippocampal tissue

(A and B) Fluorescence time-lapse images of the dendritic spines (A) and the time course of their volume changes (B) of CA1 neurons in DIV 7 hippocampal slice culture. See Videos S5, S6, and S7. Spines (asterisks) of neurons expressing control miRNA (top), shootin1 miRNA 1 (middle), or shootin1 miRNA 1 + RNAi-refractory shootin1a (bottom) were stimulated by two-photon glutamate uncaging for 30 s (0–30 s). The spine volumes were calculated by measuring the total fluorescence intensity (F) of spine heads relative to the averaged baseline fluorescence intensity (F_0), and were compared with the average of spine volumes before stimulation (−12 to 0 min).

(C) Average volume changes of dendritic spines at 1–2 min (left) and 21–31 min (right) after the stimulation in (A). For 1–2 min, one-way ANOVA, $F_{2,43} = 12.69$, $p = 4.7 \times 10^{-5}$, Tukey's post hoc test, $p = 7.8 \times 10^{-5}$ (control versus shootin1a RNAi); $p = 0.0011$ (shootin1a RNAi versus shootin1a RNAi + shootin1a); $p = 0.69$ (control versus shootin1a RNAi + shootin1a). For 21–31 min, one-way ANOVA, $F_{2,43} = 6.783$, $p = 0.0028$, Tukey's post hoc test, $p = 0.0065$ (control versus shootin1a RNAi); $p = 0.0092$ (shootin1a RNAi versus shootin1a RNAi + shootin1a); $p = 0.99$ (control versus shootin1a RNAi + shootin1a) (control RNAi, n = 15 neurons, 15 spines; shootin1a RNAi, n = 16 neurons, 16 spines; shootin1a RNAi + shootin1a, n = 15 neurons, 15 spines).

(D and E) A mechanical model for activity-induced spine structural plasticity. F-actins polymerize in the peripheral region of dendritic spines (asterisks) (D) and undergo retrograde flow from the periphery toward the center (white arrow). Synaptic activation by glutamate promotes both actin polymerization (blue arrow) and shootin1a-mediated actin-adhesion coupling (red arrow) in spines (D). The accelerated actin polymerization is required for production of force to push against the membrane (pink arrows). On the other hand, the enhanced actin-adhesion coupling reduces the speed of the F-actin retrograde flow (white arrows), thereby increasing the efficiency of the conversion of actin polymerization into force that pushes the spine membrane (pink arrows) (D). In the absence of shootin1a-mediated actin-adhesion coupling (E), the actin polymerization accelerated by the synaptic activation (asterisks) is almost entirely converted to an increase in actin retrograde flow (white arrow), thereby hampering the activity-dependent spine enlargement. For simplicity, cortactin and detailed signaling pathways are not described.

Data represent means ± SEM. ***$p < 0.01$, ns, not significant. Scale bars: 1 μm.

activation of NMDAR. This will induce spine enlargement during the cLTP procedure. Thus, our data indicate that both the shootin1a-mediated actin-adhesion coupling and actin polymerization are required for the generation of force to trigger spine enlargement (Figure 7D).

We quantified these two components; the increase in the actin-adhesion coupling was monitored by the reduction in the F-actin flow velocity, whereas the actin-polymerization rate was monitored as the sum of the F-actin protrusion rate and the F-actin retrograde flow velocity (Figure 4). On laminin, the decrease in the F-actin retrograde flow velocity and the increase in the actin polymerization rate during cLTP were 0.40 and 0.62 μm/min, respectively; on N-cadherin, they were 0.37 and 0.42 μm/min, respectively. Thus, we estimate that the relative contribution of actin-adhesion coupling and actin polymerization to the spine enlargement

was 39:61 on laminin and 47:53 on N-cadherin, respectively, revealing a large contribution of actin-adhesion coupling to trigger the spine plasticity. Quantitative data of actin-adhesion coupling, actin dynamics, and force generation in spines would enable future mechano- and systems-biological analyses of activity-dependent spine enlargement, using computational modeling, for a better understanding of synaptic plasticity.

The spine machinery identified here is also under the regulation of the molecules that control actin assembly, such as the Arp2/3 complex, formin, and profilin, and their upstream signaling pathways, including the NMDAR (Figure 7D, black arrows), as well as the molecules that control actin disassembly, such as ADF/cofilin (Hotulainen and Hoogenraad, 2010; Bosch et al., 2014; Nishiyama and Yasuda, 2015; Noguchi et al., 2016; Lei et al., 2017). Rac1 and Cdc42 are activators of Pak1-mediated shootin1a phosphorylation (Manser et al., 1994; Toriyama et al., 2013). Previous studies reported that transient stimulation of glutamate receptors by glutamate uncaging induced rapid activation of Rac1 and Cdc42 in spines, which sustained for more than 30 min (Nishiyama and Yasuda, 2015; Saneyoshi et al., 2019). Likewise, our glutamate-uncaging analyses showed that shootin1a is required not only for the initial phase but also for the sustained phase of structural LTP, suggesting that the present system also contributes to the persistence of spine enlargement under Rac1 and Cdc42. In later stages, multiple mechanisms, including F-actin stabilization through cofilin (Fukazawa et al., 2003; Bosch et al., 2014; Noguchi et al., 2016) and F-actin crosslinking by actin crosslinking proteins, such as CaMKII (Kim et al., 2015), would stabilize and maintain the enlarged spine structure.

The present model (Figure 7D) provides a mechanistic insight into the role of extrasynaptic cell adhesions in spine plasticity. In addition to the axon terminal that forms the synaptic contact, dendritic spines in the brain are surrounded by various tissue components, including ECM, non-presynaptic axons, dendritic shafts, and glial processes, which provide extrasynaptic adhesive substrates (Dityatev and Schachner, 2003; Sheng and Hoogenraad, 2007; Dansie and Ethell, 2011; Kasthuri et al., 2015). Laminins are localized around dendritic spines and implicated in the formation and stabilization of spines as well as in the maintenance of LTP (Tian et al., 1997; Seil, 1998; Nakagami et al., 2000; Egles et al., 2007; Omar et al., 2017). The mechanism by which laminins mediate spine morphogenesis has been explained mainly in terms of their roles as ligands for integrin signaling (Dityatev and Schachner, 2003; Ethell and Pasquale, 2005; Omar et al., 2017) or as components of the *trans*-synaptic cross-bridge that links pre- and post-synapses (Egles et al., 2007). N-cadherin is localized not only to the perisynaptic region, where it mediates synaptic contacts between axon terminals and spines (Uchida et al., 1996; Hirano and Takeichi, 2012), but also to the extrasynaptic region of dendritic spines (Figure S4A) (Uchida et al., 1996; Okamura et al., 2004; Korobova and Svitkina, 2010) as well as the surrounding cellular components, including axons, dendritic shafts, and astrocytes (Benson and Tanaka, 1998; Korobova and Svitkina, 2010; Camand et al., 2012). N-cadherin is also involved in the formation and plasticity of dendritic spines (Togashi et al., 2002; Okamura et al., 2004; Bozdagi et al., 2010; Hirano and Takeichi, 2012) and has been thought to regulate synaptic plasticity mainly through the *trans*-synaptic interaction between cadherins located in the perisynaptic region (Uchida et al., 1996; Hirano and Takeichi, 2012). On the other hand, the present study demonstrated that laminin and N-cadherin coated on glass-bottom dishes underpin spine enlargement during cLTP. Laminin and N-cadherin on the dishes interact with L1-CAM and N-cadherin localized in the extrasynaptic region (Figure 1D), but not with L1-CAM and N-cadherin, constituting the *trans*-synaptic adhesion. Thus, our data highlight the importance of extrasynaptic cell adhesions for spine enlargement and suggest that L1-CAM, laminin, and N-cadherin cooperatively contribute to shootin1a-mediated actin-adhesion coupling to promote robust spine plasticity (Figure 7D).

Dysregulation of the activity-dependent spine plasticity has been implicated in neuropsychiatric disorders (Kasai et al., 2010; Forrest et al., 2018). Interestingly, previous studies reported a potential role of Pak1 defects in cognitive deficits in Alzheimer disease (Zhao et al., 2006) and significantly reduced shootin1 expression in individuals with intellectual disability (InanlooRahatloo et al., 2019), raising the possibility that disruption of the present mechanism may cause neuropsychiatric disorders. A better understanding of the molecular machinery for structural plasticity of the spine should provide insights not only into the pathogenesis but also into new drug targets for neuropsychiatric diseases.

STAR★METHODS

Detailed methods are provided in the online version of this paper and include the following:

- KEY RESOURCES TABLE
- RESOURCE AVAILABILITY
  - Lead contact
  - Materials availability
  - Data and code availability
- EXPERIMENTAL MODEL AND SUBJECT DETAILS
  - Animals
  - Cell culture, transfection and RNAi
  - Hippocampal slice culture and transfection
- METHOD DETAILS
  - DNA constructs
  - Immunocytochemistry
  - DiI staining
  - Protein preparation
  - Immunoblot, immunoprecipitation and GST pull-down assay
  - *In vitro* binding assay
  - Chemical LTP
  - 2-Photon laser scanning microscopy and structural LTP
  - Fluorescent speckle imaging
  - Traction force microscopy
  - Analysis of dendritic spine morphology
- QUANTIFICATION AND STATISTICAL ANALYSIS

SUPPLEMENTAL INFORMATION

Supplemental information can be found online at https://doi.org/10.1016/j.celrep.2021.109130.

ACKNOWLEDGMENTS

We thank Drs. Haruo Kasai and Masatoshi Takeichi for valuable discussions, Dr. Yuichi Sakumura for comments on statistical analyses, and Mieko Ueda for editorial supports. This research was supported in part by AMED under grant nos. 21gm0810011h0005 (N.I.), JSPS KAKENHI (JP19H03223 [N.I.]; and JP22110006, JP20240032, and JP18H05434 [Y.H.]), JSPS Grants-in-Aid for Early-Career Scientists (JP19K16258 [T.M.]; and JP19K16127 [K.B.]), Human Frontier Science Program grant (RGP0022/2013 [Y.H.]), JST CREST (JPMJCR20E4 [Y.H.]), and the Osaka Medical Research Foundation for Incurable Diseases (T.M. and K.B.)

AUTHOR CONTRIBUTION

R.F.K., T.M., T.S., H.K.-K., Y.H., and N.I. designed the experiments. R.F.K., T.M., K.B., T.S., H.K.-K., and S.S. performed the experiments and data analysis. R.F.K., T.M., K.B., and N.I. wrote the manuscript. N.I. supervised the project. All authors discussed the results and commented on the manuscript.

DECLARATION OF INTERESTS

The authors declare no competing interests.

Received: November 2, 2020
Revised: March 9, 2021
Accepted: April 22, 2021
Published: May 18, 2021

REFERENCES

Abe, K., Katsuno, H., Toriyama, M., Baba, K., Mori, T., Hakoshima, T., Kanemura, Y., Watanabe, R., and Inagaki, N. (2018). Grip and slip of L1-CAM on adhesive substrates direct growth cone haptotaxis. Proc. Natl. Acad. Sci. USA *115*, 2764–2769.

Arikkath, J., and Reichardt, L.F. (2008). Cadherins and catenins at synapses: roles in synaptogenesis and synaptic plasticity. Trends Neurosci. *31*, 487–494.

Baba, K., Yoshida, W., Toriyama, M., Shimada, T., Manning, C.F., Saito, M., Kohno, K., Trimmer, J.S., Watanabe, R., and Inagaki, N. (2018). Gradient-reading and mechano-effector machinery for netrin-1-induced axon guidance. eLife *7*, e34593.

Benson, D.L., and Tanaka, H. (1998). N-cadherin redistribution during synaptogenesis in hippocampal neurons. J. Neurosci. *18*, 6892–6904.

Bosch, M., and Hayashi, Y. (2012). Structural plasticity of dendritic spines. Curr. Opin. Neurobiol. *22*, 383–388.

Bosch, M., Castro, J., Saneyoshi, T., Matsuno, H., Sur, M., and Hayashi, Y. (2014). Structural and molecular remodeling of dendritic spine substructures during long-term potentiation. Neuron *82*, 444–459.

Bourne, J.N., and Harris, K.M. (2008). Balancing structure and function at hippocampal dendritic spines. Annu. Rev. Neurosci. *31*, 47–67.

Bozdagi, O., Wang, X.B., Nikitczuk, J.S., Anderson, T.R., Bloss, E.B., Radice, G.L., Zhou, Q., Benson, D.L., and Huntley, G.W. (2010). Persistence of coordinated long-term potentiation and dendritic spine enlargement at mature hippocampal CA1 synapses requires N-cadherin. J. Neurosci. *30*, 9984–9989.

Camand, E., Peglion, F., Osmani, N., Sanson, M., and Etienne-Manneville, S. (2012). N-cadherin expression level modulates integrin-mediated polarity and strongly impacts on the speed and directionality of glial cell migration. J. Cell Sci. *125*, 844–857.

Chazeau, A., Mehidi, A., Nair, D., Gautier, J.J., Leduc, C., Chamma, I., Kage, F., Kechkar, A., Thoumine, O., Rottner, K., et al. (2014). Nanoscale segregation of actin nucleation and elongation factors determines dendritic spine protrusion. EMBO J. *33*, 2745–2764.

Cingolani, L.A., and Goda, Y. (2008). Actin in action: the interplay between the actin cytoskeleton and synaptic efficacy. Nat. Rev. Neurosci. *9*, 344–356.

Dansie, L.E., and Ethell, I.M. (2011). Casting a net on dendritic spines: the extracellular matrix and its receptors. Dev. Neurobiol. *71*, 956–981.

Dityatev, A., and Schachner, M. (2003). Extracellular matrix molecules and synaptic plasticity. Nat. Rev. Neurosci. *4*, 456–468.

Dityatev, A., Schachner, M., and Sonderegger, P. (2010). The dual role of the extracellular matrix in synaptic plasticity and homeostasis. Nat. Rev. Neurosci. *11*, 735–746.

Egles, C., Claudepierre, T., Manglapus, M.K., Champliaud, M.F., Brunken, W.J., and Hunter, D.D. (2007). Laminins containing the β2 chain modulate the precise organization of CNS synapses. Mol. Cell. Neurosci. *34*, 288–298.

Ethell, I.M., and Pasquale, E.B. (2005). Molecular mechanisms of dendritic spine development and remodeling. Prog. Neurobiol. *75*, 161–205.

Forrest, M.P., Parnell, E., and Penzes, P. (2018). Dendritic structural plasticity and neuropsychiatric disease. Nat. Rev. Neurosci. *19*, 215–234.

Frost, N.A., Shroff, H., Kong, H., Betzig, E., and Blanpied, T.A. (2010). Single-molecule discrimination of discrete perisynaptic and distributed sites of actin filament assembly within dendritic spines. Neuron *67*, 86–99.

Fukazawa, Y., Saitoh, Y., Ozawa, F., Ohta, Y., Mizuno, K., and Inokuchi, K. (2003). Hippocampal LTP is accompanied by enhanced F-actin content within the dendritic spine that is essential for late LTP maintenance in vivo. Neuron *38*, 447–460.

Harris, K.M., and Stevens, J.K. (1989). Dendritic spines of CA 1 pyramidal cells in the rat hippocampus: serial electron microscopy with reference to their biophysical characteristics. J. Neurosci. *9*, 2982–2997.

Hayashi, Y., and Majewska, A.K. (2005). Dendritic spine geometry: functional implication and regulation. Neuron *46*, 529–532.

Hedrick, N.G., Harward, S.C., Hall, C.E., Murakoshi, H., McNamara, J.O., and Yasuda, R. (2016). Rho GTPase complementation underlies BDNF-dependent homo- and heterosynaptic plasticity. Nature *538*, 104–108.

Hirano, S., and Takeichi, M. (2012). Cadherins in brain morphogenesis and wiring. Physiol. Rev. *92*, 597–634.

Holtmaat, A., and Svoboda, K. (2009). Experience-dependent structural synaptic plasticity in the mammalian brain. Nat. Rev. Neurosci. *10*, 647–658.

Honkura, N., Matsuzaki, M., Noguchi, J., Ellis-Davies, G.C., and Kasai, H. (2008). The subspine organization of actin fibers regulates the structure and plasticity of dendritic spines. Neuron *57*, 719–729.

Hotulainen, P., and Hoogenraad, C.C. (2010). Actin in dendritic spines: connecting dynamics to function. J. Cell Biol. *189*, 619–629.

Hotulainen, P., Llano, O., Smirnov, S., Tanhuanpää, K., Faix, J., Rivera, C., and Lappalainen, P. (2009). Defining mechanisms of actin polymerization and depolymerization during dendritic spine morphogenesis. J. Cell Biol. *185*, 323–339.

Hruska, M., Henderson, N., Le Marchand, S.J., Jafri, H., and Dalva, M.B. (2018). Synaptic nanomodules underlie the organization and plasticity of spine synapses. Nat. Neurosci. *21*, 671–682.

Inagaki, N., Nishizawa, M., Arimura, N., Yamamoto, H., Takeuchi, Y., Miyamoto, E., Kaibuchi, K., and Inagaki, M. (2000). Activation of Ca^{2+}/calmodulin-dependent protein kinase II within post-synaptic dendritic spines of cultured hippocampal neurons. J. Biol. Chem. *275*, 27165–27171.

InanlooRahatloo, K., Peymani, F., Kahrizi, K., and Najmabadi, H. (2019). Whole-transcriptome analysis reveals dysregulation of actin-cytoskeleton pathway in intellectual disability patients. Neuroscience *404*, 423–444.

Kamiguchi, H., and Yoshihara, F. (2001). The role of endocytic l1 trafficking in polarized adhesion and migration of nerve growth cones. J. Neurosci. *21*, 9194–9203.

Kasai, H., Fukuda, M., Watanabe, S., Hayashi-Takagi, A., and Noguchi, J. (2010). Structural dynamics of dendritic spines in memory and cognition. Trends Neurosci. *33*, 121–129.

Kasthuri, N., Hayworth, K.J., Berger, D.R., Schalek, R.L., Conchello, J.A., Knowles-Barley, S., Lee, D., Vázquez-Reina, A., Kaynig, V., Jones, T.R., et al. (2015). Saturated reconstruction of a volume of neocortex. Cell *162*, 648–661.

Katsuno, H., Toriyama, M., Hosokawa, Y., Mizuno, K., Ikeda, K., Sakumura, Y., and Inagaki, N. (2015). Actin migration driven by directional assembly and disassembly of membrane-anchored actin filaments. Cell Rep. *12*, 648–660.

Kim, K., Lakhanpal, G., Lu, H.E., Khan, M., Suzuki, A., Hayashi, M.K., Narayanan, R., Luyben, T.T., Matsuda, T., Nagai, T., et al. (2015). A temporary gating of actin remodeling during synaptic plasticity consists of the interplay between the kinase and structural functions of CaMKII. Neuron *87*, 813–826.

Kirov, S.A., Goddard, C.A., and Harris, K.M. (2004). Age-dependence in the homeostatic upregulation of hippocampal dendritic spine number during blocked synaptic transmission. Neuropharmacology *47*, 640–648.

Korobova, F., and Svitkina, T. (2010). Molecular architecture of synaptic actin cytoskeleton in hippocampal neurons reveals a mechanism of dendritic spine morphogenesis. Mol. Biol. Cell *21*, 165–176.

Kubo, Y., Baba, K., Toriyama, M., Minegishi, T., Sugiura, T., Kozawa, S., Ikeda, K., and Inagaki, N. (2015). Shootin1-cortactin interaction mediates signal-force transduction for axon outgrowth. J. Cell Biol. *210*, 663–676.

Lamprecht, R., and LeDoux, J. (2004). Structural plasticity and memory. Nat. Rev. Neurosci. *5*, 45–54.

Lee, S.J., Escobedo-Lozoya, Y., Szatmari, E.M., and Yasuda, R. (2009). Activation of CaMKII in single dendritic spines during long-term potentiation. Nature *458*, 299–304.

Lei, W., Omotade, O.F., Myers, K.R., and Zheng, J.Q. (2016). Actin cytoskeleton in dendritic spine development and plasticity. Curr. Opin. Neurobiol. *39*, 86–92.

Lei, W., Myers, K.R., Rui, Y., Hladyshau, S., Tsygankov, D., and Zheng, J.Q. (2017). Phosphoinositide-dependent enrichment of actin monomers in dendritic spines regulates synapse development and plasticity. J. Cell Biol. *216*, 2551–2564.

Levy, A.D., Omar, M.H., and Koleske, A.J. (2014). Extracellular matrix control of dendritic spine and synapse structure and plasticity in adulthood. Front. Neuroanat. *8*, 116.

Lu, W., Man, H., Ju, W., Trimble, W.S., MacDonald, J.F., and Wang, Y.T. (2001). Activation of synaptic NMDA receptors induces membrane insertion of new AMPA receptors and LTP in cultured hippocampal neurons. Neuron *29*, 243–254.

Manser, E., Leung, T., Salihuddin, H., Zhao, Z.S., and Lim, L. (1994). A brain serine/threonine protein kinase activated by Cdc42 and Rac1. Nature *367*, 40–46.

Matsuzaki, M., Honkura, N., Ellis-Davies, G.C., and Kasai, H. (2004). Structural basis of long-term potentiation in single dendritic spines. Nature *429*, 761–766.

Matus, A. (2000). Actin-based plasticity in dendritic spines. Science *290*, 754–758.

Minegishi, T., Uesugi, Y., Kaneko, N., Yoshida, W., Sawamoto, K., and Inagaki, N. (2018). Shootin1b mediates a mechanical clutch to produce force for neuronal migration. Cell Rep. *25*, 624–639.e6.

Mitchison, T., and Kirschner, M. (1988). Cytoskeletal dynamics and nerve growth. Neuron *1*, 761–772.

Müller, W., and Connor, J.A. (1991). Dendritic spines as individual neuronal compartments for synaptic Ca2+ responses. Nature *354*, 73–76.

Murakoshi, H., Wang, H., and Yasuda, R. (2011). Local, persistent activation of Rho GTPases during plasticity of single dendritic spines. Nature *472*, 100–104.

Nakagami, Y., Abe, K., Nishiyama, N., and Matsuki, N. (2000). Laminin degradation by plasmin regulates long-term potentiation. J. Neurosci. *20*, 2003–2010.

Nishiyama, J., and Yasuda, R. (2015). Biochemical computation for spine structural plasticity. Neuron *87*, 63–75.

Noguchi, J., Hayama, T., Watanabe, S., Ucar, H., Yagishita, S., Takahashi, N., and Kasai, H. (2016). State-dependent diffusion of actin-depolymerizing factor/cofilin underlies the enlargement and shrinkage of dendritic spines. Sci. Rep. *6*, 32897.

Okamoto, K., Nagai, T., Miyawaki, A., and Hayashi, Y. (2004). Rapid and persistent modulation of actin dynamics regulates postsynaptic reorganization underlying bidirectional plasticity. Nat. Neurosci. *7*, 1104–1112.

Okamura, K., Tanaka, H., Yagita, Y., Saeki, Y., Taguchi, A., Hiraoka, Y., Zeng, L.H., Colman, D.R., and Miki, N. (2004). Cadherin activity is required for activity-induced spine remodeling. J. Cell Biol. *167*, 961–972.

Omar, M.H., Kerrisk Campbell, M., Xiao, X., Zhong, Q., Brunken, W.J., Miner, J.H., Greer, C.A., and Koleske, A.J. (2017). CNS neurons deposit laminin α5 to stabilize synapses. Cell Rep. *21*, 1281–1292.

Park, M., Penick, E.C., Edwards, J.G., Kauer, J.A., and Ehlers, M.D. (2004). Recycling endosomes supply AMPA receptors for LTP. Science *305*, 1972–1975.

Pollard, T.D., and Borisy, G.G. (2003). Cellular motility driven by assembly and disassembly of actin filaments. Cell *112*, 453–465.

Risher, W.C., Ustunkaya, T., Singh Alvarado, J., and Eroglu, C. (2014). Rapid Golgi analysis method for efficient and unbiased classification of dendritic spines. PLoS ONE *9*, e107591.

Roberts, T.F., Tschida, K.A., Klein, M.E., and Mooney, R. (2010). Rapid spine stabilization and synaptic enhancement at the onset of behavioural learning. Nature *463*, 948–952.

Saneyoshi, T., Matsuno, H., Suzuki, A., Murakoshi, H., Hedrick, N.G., Agnello, E., O'Connell, R., Stratton, M.M., Yasuda, R., and Hayashi, Y. (2019). Reciprocal activation within a kinase-effector complex underlying persistence of structural LTP. Neuron *102*, 1199–1210.e6.

Seil, F.J. (1998). The extracellular matrix molecule, laminin, induces purkinje cell dendritic spine proliferation in granule cell depleted cerebellar cultures. Brain Res. *795*, 112–120.

Sheng, M., and Hoogenraad, C.C. (2007). The postsynaptic architecture of excitatory synapses: a more quantitative view. Annu. Rev. Biochem. *76*, 823–847.

Shimada, T., Toriyama, M., Uemura, K., Kamiguchi, H., Sugiura, T., Watanabe, N., and Inagaki, N. (2008). Shootin1 interacts with actin retrograde flow and L1-CAM to promote axon outgrowth. J. Cell Biol. *181*, 817–829.

Spence, E.F., and Soderling, S.H. (2015). Actin out: regulation of the synaptic cytoskeleton. J. Biol. Chem. *290*, 28613–28622.

Suter, D.M., and Forscher, P. (2000). Substrate-cytoskeletal coupling as a mechanism for the regulation of growth cone motility and guidance. J. Neurobiol. *44*, 97–113.

Tatavarty, V., Kim, E.J., Rodionov, V., and Yu, J. (2009). Investigating subspine actin dynamics in rat hippocampal neurons with super-resolution optical imaging. PLoS ONE *4*, e7724.

Tatavarty, V., Das, S., and Yu, J. (2012). Polarization of actin cytoskeleton is reduced in dendritic protrusions during early spine development in hippocampal neuron. Mol. Biol. Cell *23*, 3167–3177.

Tian, M., Hagg, T., Denisova, N., Knusel, B., Engvall, E., and Jucker, M. (1997). Laminin-α2 chain-like antigens in CNS dendritic spines. Brain Res. *764*, 28–38.

Togashi, H., Abe, K., Mizoguchi, A., Takaoka, K., Chisaka, O., and Takeichi, M. (2002). Cadherin regulates dendritic spine morphogenesis. Neuron *35*, 77–89.

Toriyama, M., Shimada, T., Kim, K.B., Mitsuba, M., Nomura, E., Katsuta, K., Sakumura, Y., Roepstorff, P., and Inagaki, N. (2006). Shootin1: a protein involved in the organization of an asymmetric signal for neuronal polarization. J. Cell Biol. *175*, 147–157.

Toriyama, M., Kozawa, S., Sakumura, Y., and Inagaki, N. (2013). Conversion of a signal into forces for axon outgrowth through Pak1-mediated shootin1 phosphorylation. Curr. Biol. *23*, 529–534.

Uchida, N., Honjo, Y., Johnson, K.R., Wheelock, M.J., and Takeichi, M. (1996). The catenin/cadherin adhesion system is localized in synaptic junctions bordering transmitter release zones. J. Cell Biol. *135*, 767–779.

Yuste, R. (2010). Dendritic Spines (MIT Press).

Yuste, R., and Bonhoeffer, T. (2001). Morphological changes in dendritic spines associated with long-term synaptic plasticity. Annu. Rev. Neurosci. *24*, 1071–1089.

Yuste, R., Majewska, A., and Holthoff, K. (2000). From form to function: calcium compartmentalization in dendritic spines. Nat. Neurosci. *3*, 653–659.

Zhao, L., Ma, Q.L., Calon, F., Harris-White, M.E., Yang, F., Lim, G.P., Morihara, T., Ubeda, O.J., Ambegaokar, S., Hansen, J.E., et al. (2006). Role of p21-activated kinase pathway defects in the cognitive deficits of Alzheimer disease. Nat. Neurosci. *9*, 234–242.

STAR★METHODS

KEY RESOURCES TABLE

REAGENT or RESOURCE	SOURCE	IDENTIFIER
Antibodies		
Rabbit polyclonal anti-shootin1	(Toriyama et al., 2006)	N/A
Rabbit polyclonal anti-shootin1a	(Baba et al., 2018)	N/A
Rabbit polyclonal anti-pSer101-shootin1	(Toriyama et al., 2013)	N/A
Rabbit polyclonal anti-pSer249-shootin1	(Toriyama et al., 2013)	N/A
Rabbit polyclonal anti-GFP	MBL	Cat# 598; RRID: AB_591816
Rabbit polyclonal anti-Myc tag	MBL	Cat# 562-5; RRID:AB_591116
Goat polyclonal anti-GST tag	GE Healthcare	Cat# 27-4577-01; RRID: AB_771432
Goat polyclonal anti-NCAM-L1 (c-20)	Santa Cruz Biotechnology	Cat# sc-1508; RRID: AB_631086
Rabbit monoclonal anti-N-cadherin (D4R1H)	Cell Signaling Technology	Cat# 13116 RRID: AB_2687616
Mouse monoclonal anti-cortactin p80/85 clone 4F11	Millipore	Cat# 05-180; RRID: AB_309647
Mouse monoclonal anti-actin clone C4	Millipore	Cat# MAB1501R; RRID: AB_2223041
Mouse monoclonal anti-PSD-95, 6G6-1C9	Thermo Fischer Scientific	Cat# MA1-045 RRID: AB_325399
Alexa Fluor 594 conjugated donkey anti-rabbit	Jackson Immuno Research Laboratories	Cat# 711-585-152; RRID: AB_ 2340621
Alexa Fluor 488 conjugated goat anti-rabbit	Thermo Fisher Scientific	Cat# A-11008; RRID: AB_143165
Alexa Fluor 488 conjugated goat anti-mouse	Thermo Fisher Scientific	Cat# A-11029; RRID: AB_2534088
Alexa Fluor 488 conjugated donkey anti-goat	Thermo Fisher Scientific	Cat# A-11055; RRID: AB_ 2534102
HRP conjugated donkey anti-rabbit	GE Healthcare	Cat# NA934; RRID: AB_772206
HRP conjugated donkey anti-goat	Millipore	Cat# AP180P; RRID: AB_92573
HRP conjugated goat anti-mouse	Bio-Rad	Cat# 1706516; RRID: AB_11125547
Chemicals, peptides, and recombinant proteins		
Alexa Fluor 594 conjugated phalloidin	Thermo Fisher Scientific	Cat# A12381
Alexa Fluor 350 conjugated phalloidin	Thermo Fisher Scientific	Cat# A22281
Poly-D-lysine hydrobromide	Sigma	Cat# P6407-5MG
Laminin solution from mouse EHS tumor	Wako	Cat# 120-05751
N-cadherin-Fc	(Kamiguchi and Yoshihara, 2001)	N/A
HaloTag TMR ligand	Promega	Cat# G8251
PhosSTOP	Roche	Cat# 4906845001
NVS PAK1-1	Sigma	Cat# SML1867-5MG
L-Glutamic Acid	Nacalai Tesque	Cat#13012-92
MNI-caged-glutamate	Tocris	Cat# 1490
Tetrodotoxin	Wako	Cat# 206-11071
Picrotoxin	Nacalai Tesque	Cat# 28004-71
Bicuculin	Tocris	Cat# 0130
Strychnine	Nacalai Tesque	Cat# 32316-74
Glycine	Nacalai Tesque	Cat# 09591-55
D-2-amino-5-phosphonovalerate	Hello Bio	Cat# HB0225
MK-801	Hello Bio	Cat# HB0004
Gluthathione Sepharose 4B	GE Healthcare	Cat# 17-0756-01

(*Continued on next page*)

Continued

REAGENT or RESOURCE	SOURCE	IDENTIFIER
Critical commercial assays		
Protein G Sepharose 4 Fast Flow	GE Healthcare	Cat# 17-0618-01
DiI stain	Thermo Fisher Scientific	Cat# D3911
Rat Neuron Nucleofector Kit (25RCT)	Lonza	Cat# VPG-1003
Lipofectamine 2000	Thermo Fisher Scientific	Cat# 11668027
Polyethylenimine MAX	Polyscience	Cat# 24765-1
Deposited data		
Data S1	This study	https://dx.doi.org/10.17632/yjv7ts2s3z.3
Experimental models: cell lines		
HEK293T cell	ATCC	Cat# CRL_3216; RRID:CVCL_0063
Experimental models: organisms/strains		
Mouse C57BL/6	Japan SLC; CLEA Japan	N/A
Mouse Shootin1 KO	(Baba et al., 2018)	N/A
Rat Wistar	Japan SLC; CLEA Japan	N/A
Rat Sprague-Dawley	Japan SLC; CLEA Japan	N/A
Oligonucleotides		
Genotyping F1 5′-CAGACT GCTACCCACTACCCCCTAC-3′	(Baba et al., 2018)	N/A
Genotyping R1 5′-CCTAGAG CTGGACAGCGGATCTGAG-3′	(Baba et al., 2018)	N/A
Genotyping F2 5′-CCCAGAA AGCGAAGGAACAAAGCTG-3′	(Baba et al., 2018)	N/A
Genotyping R2 5′-ACCTTGC TCCTTCAAGCTGGTGATG-3′	(Baba et al., 2018)	N/A
Shootin1a (30-146) F 5′-ATCTTCA GATCTGAGAACCAGAAA ACAAAGGAGACG-3′	This study	N/A
Shootin1a (30-146) R 5′-GCCG CCTCGAGTTATTCTTTGAT TTGCTTCTGACACTG-3′	This study	N/A
Lifeact top 5′-TCGAGATGGGTG TCGCAGATTTGATCAAGAAATTC GAAAGCATCTCAAAGGAAGAAGGG-3′	This study	N/A
Lifeact bottom 5′-GATCCCTTCTTC CTTTGAGATGCTTTCGAATTTCTT GATCAAATCTGCGACACCCATC-3′	This study	N/A
N-cadherin ICD F 5′-AAAGGATCCA TGAAACGCCGGGATAAAG-3′	This study	N/A
N-cadherin ICD R 5′-AAAGTCGAC CTAGTCATCACCTCCACCATACATG-3′	This study	N/A
Shootin1a F 5′-ATATGCGATCG CCATGAACAGCTCGGA-3′	This study	N/A
Shootin1a R 5′-AAACGTTTAAA CCTGGGAGGCCAGGATT-3′	This study	N/A
Recombinant DNA		
pCAGGS -myc-GST	(Toriyama et al., 2006)	N/A
pCAGGS-myc-shootin1(1-125)	(Baba et al., 2018)	N/A
pCAGGS-myc-shootin1a(30-146)	This study	N/A
pGEX-6P-1	GE Healthcare	Cat# 28954648
pCMV-myc-shootin1a	(Toriyama et al., 2006)	N/A

(*Continued on next page*)

Continued

REAGENT or RESOURCE	SOURCE	IDENTIFIER
pCAGGS-myc-GST	(Toriyama et al., 2006)	N/A
pCAGGS-myc-shootin1a	(Toriyama et al., 2006)	N/A
pCMV-EGFP	(Katsuno et al., 2015)	N/A
pCMV-EGFP-shootin1a	(Katsuno et al., 2015)	N/A
pCMV-EGFP-shootin1a(1-125)	(Baba et al., 2018)	N/A
pCMV-EGFP-shootin1a(30-146)	This study	N/A
pCMV-EGFP-shootin1a(125-260)	(Shimada et al., 2008)	N/A
pCMV-EGFP-shootin1a(217-456)	(Shimada et al., 2008)	N/A
pCMV-myc-shootin1a	(Toriyama et al., 2006)	N/A
pGEX-N-cadherin-ICD(intracellular domain)	This study	N/A
pFN21A-HaloTag-actin	(Minegishi et al., 2018)	N/A
pFN21A-HaloTag-cortactin	(Minegishi et al., 2018)	N/A
pFN21A-HaloTag-shootin1a	This study	N/A
pCMV-myc-shootin1 refractory	(Shimada et al., 2008)	N/A
pmNeonGreen-N1-lifeact	This study	N/A
Software and algorithms		
ImageJ software	National Institutes of Health	https://imagej.nih.gov/ij/index.html; RRID: SCR_003070
GraphPad Prism7	GraphPad Software	https://www.graphpad.com/; RRID: SCR_002798
Axiovison3	Carl Zeiss	http://www.usask.ca/biology/scopes/AxioVision%204-7-2%20Takeoff%20Guide.pdf; RRID: SCR_002677
ZEN software	Carl Zeiss	https://www.zeiss.com/microscopy/int/products/microscope-software/zen.html; RRID: SCR_013672
FV10-ASW	Olympus	https://www.photonics.com/Products/FV10-ASW_30_Software/p6/v081/i539/pr47380; RRID: SCR_014215

RESOURCE AVAILABILITY

Lead contact

Further information and requests for resources and reagents should be directed to and will be fulfilled by the Lead Contact, Naoyuki Inagaki (ninagaki@bs.naist.jp).

Materials availability

All unique materials generated in this study are available from the Lead contact with a completed Materials Transfer Agreement.

Data and code availability

Source data of immunostaining, immunoblot and statistical analyses in the figures are available at Mendeley Data (https://doi.org/10.17632/yjv7ts2s3z.3). Owing to large size of datasets generated and analyzed in this study, other datasets are available from the corresponding author on request.

EXPERIMENTAL MODEL AND SUBJECT DETAILS

Animals

All relevant aspects of the experimental procedures were approved by the Institutional Animal Care and Use Committee of Nara Institute of Science and Technology and Kyoto University Graduate School of Medicine. Embryonic stages were calculated from noon of the vaginal plug day, which was defined as embryonic day 0.5 (E0.5). E18 Wistar pregnant rats and P6–8 Sprague-Dawley rats were obtained from Japan SLC and CLEA Japan. E16.5 shootin1 KO embryos and P12 shootin1 KO pups were obtained by crossing male and female shootin1 heterozygous C57BL/6 mice. Shootin1 KO pups and the littermates were bred with their mother under standard

conditions (12 h/12 h light/dark cycle, access to dry food and water). Mice and rats of both sexes in each developmental stage and at each age were used for experiments.

The generation of shootin1 knockout mice is described elsewhere (Baba et al., 2018). Chimeric mice were crossed with C57BL/6 mice for at least seven generations before analysis. Male and female shootin1 heterozygous mice were mated to obtain shootin1 KO mice; the offspring genotypes were checked by PCR with the following primers: Genotyping F1 (5′-CAGACTGCTACCCACTAC CCCCTAC-3′),

Genotyping R1 (5′-CCTAGAGCTGGACAGCGGATCTGAG-3′),
Genotyping F2 (5′-CCCAGAAAGCGAAGGAACAAAGCTG-3′),
Genotyping R2 (5′-ACCTTGCTCCTTCAAGCTGGTGATG-3′).

Cell culture, transfection and RNAi

Hippocampal neurons prepared from E18 rats were cultured on glass coverslips (Matsunami) or glass bottom dishes (Matsunami) coated with PDL or coated sequentially with PDL and laminin as reported (Inagaki et al., 2000; Shimada et al., 2008). For the experiments in Figures 4E, 4F, 6A, 6C, and S4A, neurons were cultured on glass coverslips or glass bottom dishes coated sequentially with PDL and N-cadherin-Fc (Kamiguchi and Yoshihara, 2001). For the immunoprecipitation analyses in Figures 3D and 3F, we used neurons prepared from E18 rat cerebral cortex, which were also used for cLTP experiments (Hruska et al., 2018), as the experiments required large numbers of neurons. For the analyses in Figure 2D, hippocampal neurons prepared from E16.5 WT and shootin1 KO mice were used. They were prepared using the same protocol as above. All experiments except for the traction force microcopy were carried out on glass surfaces. For DIV7 observations, neurons were transfected with plasmid DNA using Nucleofector (Lonza) before plating. For DIV14 and DIV21 observations, neurons were transfected at DIV7 and DIV10, respectively, by Lipofectamine 2000 (Thermo Fisher Scientific) according to the manufacturer's protocol. For RNAi experiments, we used a Block-iT Pol II miR RNAi expression kit (Thermo Fisher Scientific). The targeting sequences of shootin1a miRNA #1 and #2 and the sequence of RNAi refractory shootin1a were reported previously (Toriyama et al., 2006; Shimada et al., 2008; Toriyama et al., 2013).

HEK293T cells (ATCC) were cultured in Dulbecco's modified Eagle's medium (Sigma) containing 10% FBS (Japan Bio Serum) as described previously (Baba et al., 2018) and transfected with vectors using Polyethylenimine MAX (PEI MAX, Polysciences) following the manufacturer's protocol.

Hippocampal slice culture and transfection

For the experiments of structural LTP induction in Figure 7A, hippocampal slices were prepared from P6–8 Sprague-Dawley rats as described previously (Bosch et al., 2014). After five days, the slices were transfected with vectors by a biolistic method (Gene-Gun, Bio-Rad) as described (Bosch et al., 2014).

METHOD DETAILS

DNA constructs

Preparations of the vectors to express shootin1a, shootin1a (1–125), shootin1a (125–260), and shootin1a (217–456) have been described previously (Toriyama et al., 2006; Shimada et al., 2008; Kubo et al., 2015). To generate pCAGGS-myc-shootin1a (30–146), the cDNA of human shootin1a (Toriyama et al., 2006) was amplified by PCR with the primers Shootin1a (30–146) F (5′-ATCTTC AGATCTGAGAACCAGAAAACAAAGGAGACG-3′) and Shootin1a (30–146) R (5′-GCCGCCTCGAGTTATTCTTTGATTTGCTTCTGAC ACTG-3′), and then subcloned into pCAGGS-myc vector (Toriyama et al., 2006). To generate pmNeonGreen-N1-Lifeact (fused to C-terminal mNeonGreen tag) vector, the DNA fragments Lifeact top (5′-TCGAGATGGGTGTCGCAGATTTGATCAAGAAATTCGA AAGCATCTCAAAGGAAGAAGGG-3′) and Lifeact bottom (5′-GATCCCTTCTTCCTTTGAGATGCTTTCGAATTTCTTGATCAAATCT GCGACACCCATC-3′) were annealed and inserted into pmNeonGreen-N1 (Allele Biotechnology) vectors. To generate pGEX-N-cadherin ICD (intracellular domain), the cDNA of human N-cadherin was amplified by PCR with the primers N-cadherin ICD F (5′-AAAGG ATCCATGAAACGCCGGGATAAAG-3′) and N-cadherin ICD R (5′-AAAGTCGACCTAGTCATCACCTCCACCATACATG-3′), and then subcloned into pGEX-6P-1 vector (GE Healthcare). To generate pFN21A-Halotag-shootin1a, the cDNA of human shootin1a (Toriyama et al., 2006) was amplified by PCR with the primers Shootin1a F (5′-ATATGCGATCGCCATGAACAGCTCGGA-3′) and Shootin1a R (5′-AAACGTTTAAACCTGGGAGGCCAGGATT-3′), and then subcloned into pFN21A HaloTag CMV Flexi vector (Promega). Preparations of pFN21A-HaloTag-actin and pFN21A-HaloTag-cortactin were described previously (Minegishi et al., 2018).

Immunocytochemistry

Cultured neurons were fixed with 3.7% formaldehyde in Krebs buffer (118 mM NaCl, 4.7 mM KCl, 1.2 mM KH_2PO_4, 1.2 mM $MgSO_4$, 4.2 mM $NaHCO_3$, 2 mM $CaCl_2$, 10 mM glucose, 400 mM sucrose, 10 mM HEPES pH 7.0) for 10 min at room temperature, followed by treatment for 15 min with 0.05% Triton X-100 in PBS on ice and 10% fetal bovine serum in PBS for 1 h at room temperature. They were then incubated with primary antibody diluted in PBS containing 10% fetal bovine serum overnight at 4°C. The following primary antibodies were used: rabbit anti-shootin1a (1:2,000), mouse anti-cortactin (1:500) (Millipore), goat anti-NCAM-L1 (1:500) (Santa Cruz Biotechnology), rabbit monoclonal anti-N-cadherin (D4R1H) (1:1,000) (Cell Signaling), mouse anti-PSD-95 (1:500) (Thermo Fisher

Scientific), and rabbit anti-GFP (1:500) (MBL) antibodies. Neurons were washed with PBS, and then incubated with secondary antibody diluted in PBS overnight at room temperature. The following secondary antibodies were used: Alexa Fluor 594 conjugated donkey anti-rabbit (1:1,000) (Jackson ImmunoResearch Laboratories), Alexa Fluor 488 conjugated goat anti-rabbit (1:1,000) (Thermo Fisher Scientific), Alexa Fluor 488 conjugated goat anti-mouse (1:1,000) (Thermo Fisher Scientific) and Alexa Fluor 488 conjugated donkey anti-goat (1:1,000) (Thermo Fisher Scientific) antibodies. After washing with PBS, some of the neurons were stained with Alexa Fluor 594 conjugated phalloidin (1:100) (Thermo Fisher Scientific) or Alexa Fluor 350 conjugated phalloidin (1:50) (Thermo Fisher Scientific) for 30 min at room temperature. Immunostained cells were mounted with 50% (v/v) glycerol (Nacalai Tesque) in PBS. Fluorescence images were acquired using either a fluorescence microscope (Axioplan2, Carl Zeiss) equipped with a Plan-Apochromat 63 × oil, 1.40 NA objective (Carl Zeiss), a charge-coupled device camera (CCD, AxioCam MRm, Carl Zeiss) and imaging software (Axiovision3, Carl Zeiss), or a TIRF microscope (IX81, Olympus) and imaging software (MetaMorph, Molecular Devices).

DiI staining

P12 WT and shootin1 KO mice were anesthetized with a mixture of 0.75 mg/kg medetomidine hydrochloride (Domitor, Nippon Zenyaku Kogyo), 4 mg/kg midazolam (Sandoz) and 5 mg/kg butorphanol tartrate (Bettlefar, Meiji Seika Pharma) via intraperitoneal injection (0.01 ml/g body weight) and perfused through the left ventricle with ice-cold PBS (pH 7.4) followed by 4% paraformaldehyde (PFA) in PBS. The brains were removed and postfixed in the same fixative overnight at 4°C. Serial coronal sections (200 μm) of agarose-embedded brains were cut on a vibratome (Leica) and collected in PBS. DiI (Thermo Fisher Scientific) crystals were placed on the hippocampus under a dissecting microscope. The brain sections were then incubated in 1.5% PFA at room temperature for 4–12 h to allow DiI to fully diffuse along the pyramidal neurons. Slices were then fixed with 4% PFA at room temperature for 30 minutes and mounted in 30% sucrose. Fluorescence images were acquired using a confocal microscope (LSM710, Carl Zeiss). The images of DiI-labeled dendritic filopodia and spines of CA1 hippocampal neurons were first taken as three-dimensional image stacks and then projected to two-dimensional images using the maximal intensity-z projection function of ImageJ (National Institutes of Health).

Protein preparation

Recombinant proteins were expressed in *Escherichia coli* as GST fusion proteins and purified on Glutathione Sepharose columns (GE Healthcare), after which GST was removed by PreScission protease (GE Healthcare) as described (Kubo et al., 2015). N-cadherin-Fc was prepared as described (Kamiguchi and Yoshihara, 2001).

Immunoblot, immunoprecipitation and GST pull-down assay

Immunoblot was performed as described (Toriyama et al., 2006; Baba et al., 2018). For immunoprecipitation with cultured neurons, after glutamate (10 μM) stimulation for 30 min, cell lysates were prepared with NP40–Triton lysis buffer (0.5% NP-40, 1% Triton X-100, 20 mM HEPES pH 7.5, 3 mM $MgCl_2$, 100 mM NaCl, 1 mM EGTA, 1 mM DTT, 1 mM PMSF, 0.01 mM leupeptin, 1 × PhosStop). The supernatants of the lysates were incubated with antibodies overnight at 4°C, and immunocomplexes were then precipitated with protein G-Sepharose 4B. After washing the beads with wash buffer (0.1% Tween 20, 20 mM HEPES pH 7.5, 3 mM $MgCl_2$, 100 mM NaCl, 1 mM EGTA, 1 mM DTT), immunocomplexes were analyzed by immunoblot.

For the GST pull-down assay, cell lysates of HEK293T cells were prepared using NP40 lysis buffer (0.5% NP-40, 20 mM HEPES pH 7.5, 3 mM $MgCl_2$, 100 mM NaCl, 1 mM EGTA, 1 mM DTT, 1 mM PMSF, 0.01 mM leupeptin, 1 × PhosStop) as described (Baba et al., 2018). The supernatants of cell lysates and purified GST-N-cadherin-ICD were incubated overnight at 4°C. After centrifugation for 15 min at 17,400 g at 4°C, the supernatants were incubated with Glutathione Sepharose 4B beads for 2 h at 4°C. The beads were washed three times with wash buffer (0.1% Tween 20, 20 mM HEPES pH 7.5, 3 mM $MgCl_2$, 100 mM NaCl, 1 mM EGTA, 1 mM DTT). For elution, the Sepharose beads were incubated with 25 μL of elution buffer (15 mM reduced glutathione pH 8.0, 20 mM Tris-HCl pH 8.0, 100 mM NaCl, 1 mM EDTA, 1 mM DTT) for 2 h at 4°C. The eluate was analyzed by immunoblot.

In vitro binding assay

Purified GST-N-cadherin-ICD and purified shootin1a were incubated overnight at 4°C in reaction buffer (20 mM Tris-HCl pH 8.0, 100 mM NaCl, 1 mM EDTA, 1 mM DTT). After centrifugation for 15 min at 17,400 g at 4°C, the supernatants were incubated with Glutathione Sepharose 4B beads for 2 h at 4°C. The beads were washed three times with wash buffer (20 mM Tris-HCl pH 8.0, 300 mM NaCl, 1 mM EDTA, 1 mM DTT) and once with TED buffer (20 mM Tris-HCl pH 8.0, 1 mM EDTA, 1 mM DTT). For elution, the Sepharose beads were incubated with 25 μL of elution buffer (15 mM reduced glutathione pH 8.0, 20 mM Tris-HCl pH 8.0, 100 mM NaCl, 1 mM EDTA, 1 mM DTT) for 2 h at 4°C. The eluates were analyzed by immunoblot.

Chemical LTP

NMDAR-dependent chemical LTP was performed as previously described (Hruska et al., 2018; Lu et al., 2001). DIV14 cultured hippocampal neurons were placed in artificial cerebrospinal fluid (ACSF, 143 mM NaCl, 5 mM KCl, 2 mM $CaCl_2$, 1 mM $MgCl_2$, 30 mM glucose, 10 mM HEPES, pH 7.4) containing 0.5 μM tetrodotoxin, 1 μM strychnine and 20 μM bicuculline at 37°C. After 15 min of imaging, the neurons were treated with glycine stimulation solution (ACSF without $MgCl_2$, 0.5 μM tetrodotoxin, 1 μM strychinine, 20 μM bicuculline, 200 μM glycine) for 4 min, followed by ACSF without $MgCl_2$. To block NMDAR, 50 μM D-AP5 and 10 μM MK-801 were included in the solutions described above. Fluorescence images were acquired every 5 min using a confocal microscope (LSM700 or

710, Carl Zeiss) equipped with a Plan-Apochromat 63x 1.40 oil M27 objective. To acquire and quantify each image, we obtained 8 section images along 4.62 μm thickness in the Z axis; we confirmed that the whole thickness of a spine was scanned within the 4.62 μm thickness. The 8 images were then volume-stacked and quantified.

2-Photon laser scanning microscopy and structural LTP

Structural LTP induction was performed as previously described (Bosch et al., 2014). Hippocampal slices cultured for 7 days were placed in Mg^{2+}-free ACSF containing 119 mM NaCl, 2.5 mM KCl, 3 mM $CaCl_2$, 26.2 mM $NaHCO_3$, 1 mM NaH_2PO_4, 11 mM glucose, 1 μM tetrodotoxin, 50 μM picrotoxin, and 6 mM 4-methoxy-7-nitroindolinyl (MNI)-L-glutamate aerated with 95% O_2 and 5% CO_2. Fluorescence images of primary or secondary dendrites from the distal part of the main apical dendrite of CA1 pyramidal neurons were acquired using a 2-photon microscope (FluoViewFV1000MPE, Olympus) equipped with Ti-sapphire lasers (Spectra-Physics) and imaging software (FV10-ASW, Olympus). We induced structural LTP on spines with a clear head and neck by uncaging MNI-glutamate with 2-ms laser pulses (720 nm at 5 mW under objective lens) repeated at 1 Hz for 30 pulses.

Fluorescent speckle imaging

Fluorescent speckle imaging was performed as described previously (Abe et al., 2018; Baba et al., 2018). Hippocampal neurons expressing HaloTag-actin, HaloTag-cortactin or HaloTag-shootin1a were cultured until DIV7 or DIV14 on glass bottom dishes coated with PDL + laminin or PDL + N-cadherin-Fc. Prior to observation, neurons were treated with HaloTag TMR ligand (Promega) at 1:2,000 dilution in the culture medium and incubated for 1 h at 37°C. The ligand was then washed out with PBS and the neurons were incubated in L-15 medium containing 2% B27 supplement and 1% GlutaMAX. The fluorescent speckles of HaloTag proteins were observed using a fluorescence microscope (AxioObserver Z1, Carl Zeiss) equipped with a complementary metal oxide semiconductor (CMOS, ORCA Flash4.0 V2, Hamamatsu), a Plan-Apochromat 100x, 1.40 NA (Carl Zeiss), and imaging software (ZEN 2012, Carl Zeiss). Fluorescence images were acquired every 2 s. F-actin flow velocity was calculated by tracing the speckles of HaloTag-actin. Actin polymerization rate was calculated as the sum of F-actin protrusion rate, monitored by Lifeact (green lines), and F-actin flow velocity, as reported (Katsuno et al., 2015). As typical actin speckles in mushroom spines could be traced for only about 10 s, we selected 10 s periods in time-lapse montages in which we could trace clearly the flow of actin speckle. We carefully placed a line that links the distal tips of actin filaments in the first and last frames; then, the average polymerization rate during the observation was determined. We performed similar steps in the actin flow analyses in the same time frame.

Traction force microscopy

Traction force microscopy was performed as previously reported (Toriyama et al., 2013; Abe et al., 2018) with modifications. Polyacrylamide gels with embedded fluorescent microspheres (100 nm diameter; Thermo Fisher Scientific) were prepared as described (Toriyama et al., 2013). Neurons expressing EGFP were cultured on the polyacrylamide gels, coated with PDL + laminin, until DIV7. Time-lapse imaging of fluorescent beads and dendritic filopodia was performed at 37°C using a confocal microscope (LSM710, Carl Zeiss) equipped with a C-Apochromat 63x/1.2 W Corr objective. Dendritic filopodia of transfected neurons were identified by EGFP fluorescence and DIC images. Traction forces under dendritic filopodia were monitored by visualizing force-induced deformation of the elastic substrate, which is reflected by movement of the beads from their original positions (Toriyama et al., 2013). Because of the tiny size of an individual filopodium, we could not find multiple beads under it. Therefore, the force generated by filopodia is difficult to calculate by integrating the movements of multiple beads under them (Toriyama et al., 2013; Abe et al., 2018). Instead, we measured the magnitude (μm) and direction (θ) of the movement of individual beads under the filopodia. After time-lapse imaging, the culture dishes were treated with 1% SDS to release neurons from the polyacrylamide gel substrate, and an image of the original positions of the beads was acquired.

Analysis of dendritic spine morphology

Morphological analysis of dendritic protrusions was performed based on criteria reported previously (Bourne and Harris, 2008; Risher et al., 2014) with slight modifications. The length, head width, and neck width of dendritic protrusions were measured using ImageJ, and the protrusions were classified into dendritic filopodia, thin spines, stubby spines, and mushroom spines as follows: dendritic filopodia, without head (length $\geq$ 2 μm); thin spines, with head (head width $\leq$ 0.6 μm); stubby spines: length $\leq$ width; mushroom spines, with head (head width $\geq$ 0.6 μm). Branched spines, which might represent an error of synaptic connection (Yuste, 2010), were also observed as a small population (~1%); we did not include them in the analysis.

QUANTIFICATION AND STATISTICAL ANALYSIS

All statistical analyses were performed using Excel 2016 (Microsoft) and GraphPad Prism7 (GraphPad Software). We tested normal distribution for all data by the D'Agostino–Pearson normality test. We also tested the equality of variation by F-test for two independent groups that show normal distribution. We then performed significance tests as following: (1) two-tailed paired t test for the comparison between two dependent groups that showed normal distribution; (2) Wilcoxon signed-rank test for the comparison between two dependent groups that showed non-normal distribution; (3) two-tailed unpaired Student's t test for the comparison between two independent groups that showed normal distribution and equal variation; (4) two-tailed unpaired Welch's t test for the comparison

between two independent groups that showed normal distribution and unequal variation; (5) Mann–Whitney U test for the comparison between two independent groups that showed non-normal distribution; and (6) one-way ANOVA with Tukey's post hoc test for the comparisons among three groups. For each experiment, the corresponding statistics information and number of samples are indicated in the figure legend. All data are shown as the mean ± SEM. Statistical significance was defined as ***$p < 0.01$; **$p < 0.02$; *$p < 0.05$; ns, not significant. Randomization was not performed in this study, which did not include clinical trials. For the experiments using KO mouse/embryo, littermates were allocated into each experimental group from the genotypes. For other experiments, sample allocation was random because cells and purified proteins were used from the same resource in each experiment. The numbers for groups in each sample were based on those in previously published studies. No data is excluded if the experiments were successfully performed. All experiments were done at least three times and reliably reproduced. Investigators were blind to experimental groups for each analysis, except biochemical analyses.